

The author(s) shown below used Federal funds provided by the U.S. Department of Justice and prepared the following final report:

Document Title: Compact, Low-Cost Body Cavity Screening Device

Author(s): Erik Magnuson

Document No.: 241685

Date Received: April 2013

Award Number: 2007-DE-BX-K001

This report has not been published by the U.S. Department of Justice. To provide better customer service, NCJRS has made this Federally-funded grant report available electronically.

Opinions or points of view expressed are those of the author(s) and do not necessarily reflect the official position or policies of the U.S. Department of Justice.



Final Report

Compact, Low-Cost Body Cavity Screening Device

by

Quantum Magnetics, Inc
1251 East Dyer Road, Ste. 140, Santa Ana, CA 92705-5639
Telephone 714-258-4400, Fax 714-258-4404

NIJ Cooperative Agreement No. 2007-DE-BX-K001

QM Internal Project No. CJ10811

January 2013

Principal Investigator:
Erik Magnuson
Lead Electrical Engineer
714-727-0521
FAX: 714-258-4404
EMagnuson@morphodetection.com

Administrative Point of Contact:
Ms. Quyen Tran
Sr. Contract Performance Manager
858-605-5601
FAX: 858-408-3871
QTran@morphodetection.com

Organization: Quantum Magnetics, Inc., a CA corporation and wholly-owned subsidiary of Morphodetection, Inc., 1251 East Dyer Road, Ste. 140, Santa Ana, CA 92705-5639. Phone: 714-258-4400.

Compact, Low-Cost Body Cavity Screening Device

1. Abstract

Electric field tomography (EFT) was investigated as a method for developing a low-cost, non-invasive body cavity screening device. Initial detection and operational requirements were developed from discussions with California Department of Corrections personnel and their counterparts in the western United States. A laboratory prototype system was developed with fixed receive and transmit nodes. Images were reconstructed from both experimental and simulated data and were shown to be in good agreement. In order to overcome the inherent low resolution of EFT, a novel multi-frequency method was developed where images acquired over frequency range of 1 MHz to 20 MHz were used to build a linear model and decompose the different object types (for example: muscle, bone, plastic) in the image. The feasibility of the multi-frequency EFT method was demonstrated with simulated data, and finally with actual images. The designs for new prototype employing switching transceiver nodes were finalized.

2. Executive Summary

Electric field tomography (EFT) has been investigated as a technology enabling a low-cost, non-invasive device to screen body cavities for concealed contraband. Initial requirements were developed from discussions with California Department of Corrections personnel and their counterparts in the western United States. The consultation yielded a list of initial target objects, given in Table ES-1. Detectability is a function of the contrast in dielectric constant between the object and surrounding tissue, and the goals in Table 1 are aggressive but reasonable. Note that since commercial metal detectors already exist that are capable of detecting the metallic objects, and since discrimination of plastic from human tissue is much more challenging than discriminating metal, it was decided to husband limited resources and make plastic detection and discrimination the sole objective of this phase of the effort.

Material	Detection Goal
Nonferrous metal	.22 caliber bullet
Ferrous steel	Single razor blade
Plastic	Cylinder 8 mm in diameter by 10 cm long

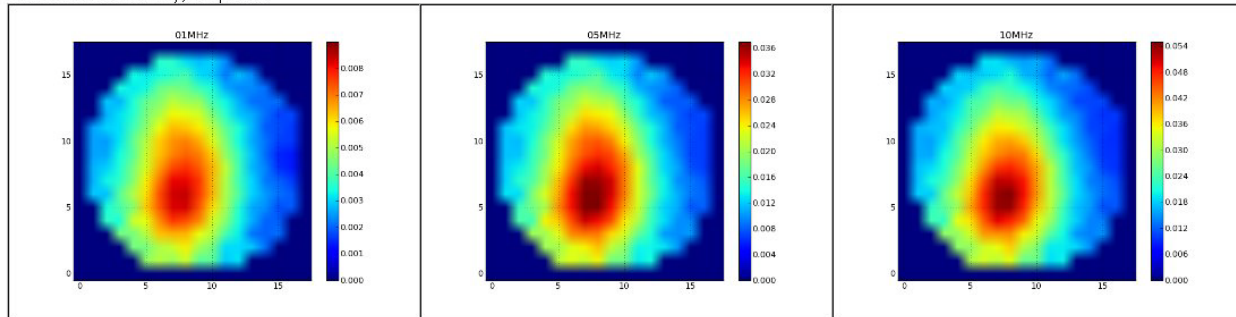
Table ES-1. Materials and detection goals for the body cavity screening system.

Operational requirements include a desire that the system not require contact with the skin (a device requiring contact would likely not be usable on visitors and other non-inmates); that it accommodate subjects up to the 95th percentile in girth; that it be stowable when not in use; that it be easy to use and provide intuitively understandable results; and that its cost be similar to the \$6,000 now paid for metal detection portals. System throughput is a lesser concern, with scan times of several tens of seconds per subject being acceptable.

Work in this phase of the project showed that imaging at a single frequency is inadequate to discriminate foreign objects from the surrounding human tissue. However, multi-frequency tomography allied with a new processing approach improves detectability substantially, close to attaining the detection goals of Table 1. Linear modeling of multi-frequency multi-object images

can be used to decompose the composite images into single-object images, enabling detection of plastic insertion objects within human tissue clutter that would not have been possible in the original composite images. The method shows promise for the use of EFT as a detector of foreign objects within a non-uniform body tissue background despite the inherent low resolution of EFT images. Figure ES-1 shows a set of composite image simulations with bone and muscle in the top row, and bone, muscle and a plastic object in the bottom row. The difference between top and bottom is not apparent. Figure ES-2 shows the same image simulations, now decomposed into separate bone, muscle and plastic components. The difference between the upper and lower plastic-component images is clear.

Bone and muscle only, no plastic



Bone, muscle and plastic

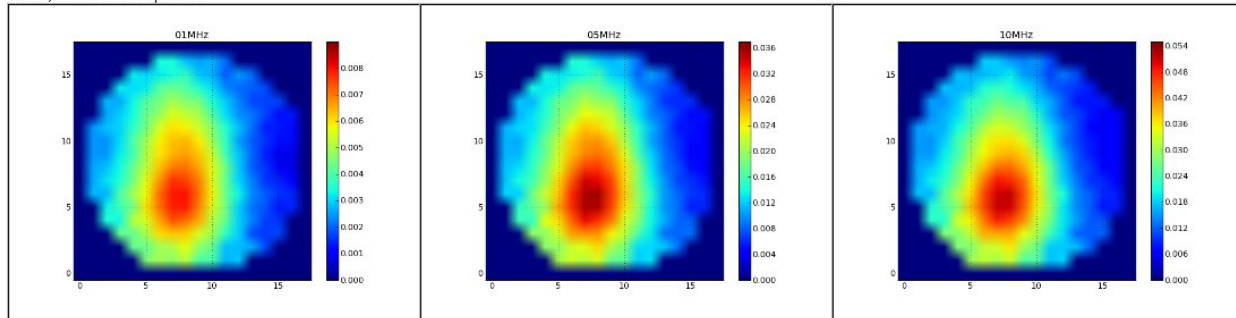


Figure ES-1. Composite images at different frequencies. Top row images are from bone and muscle simulations. Bottom row images are from bone, muscle, plastic simulations.

Work on hardware prototypes has overcome a series of technical challenges to produce multi-frequency images whose noise thresholds are near, or below, those required in the simulations. Figure ES-3 shows a set of multi-frequency measurements with low phase noise across the measurement frequency band from 1 MHz to 20 MHz. The images show the presence of the target phantom at the left center of the image (dark orange at low frequencies, shading to blue at high frequencies).

To achieve better detection sensitivity and image resolution, ultra-low-noise amplifier circuit topologies were investigated both on paper and with laboratory measurements on partial circuits. The most promising topology carries substantial risk, requiring more hardware study than supported by the current phase of the project; for this reason, the next generation of electronics retains the present, well-characterized amplifier design.

In preparation for a prototype system suitable for testing on human subjects, electronics have been designed to allow individual capacitor nodes to act as both transmitter and receiver, switching between the two on command of the operating software, to enable rapid collection of

tomographic data. The next phase of this project will fabricate, debug and implement the transceiver electronics on a laboratory prototype, validate its operation on phantoms simulating human tissue and contrabands, and finally test it on human subjects (without concealed contraband).

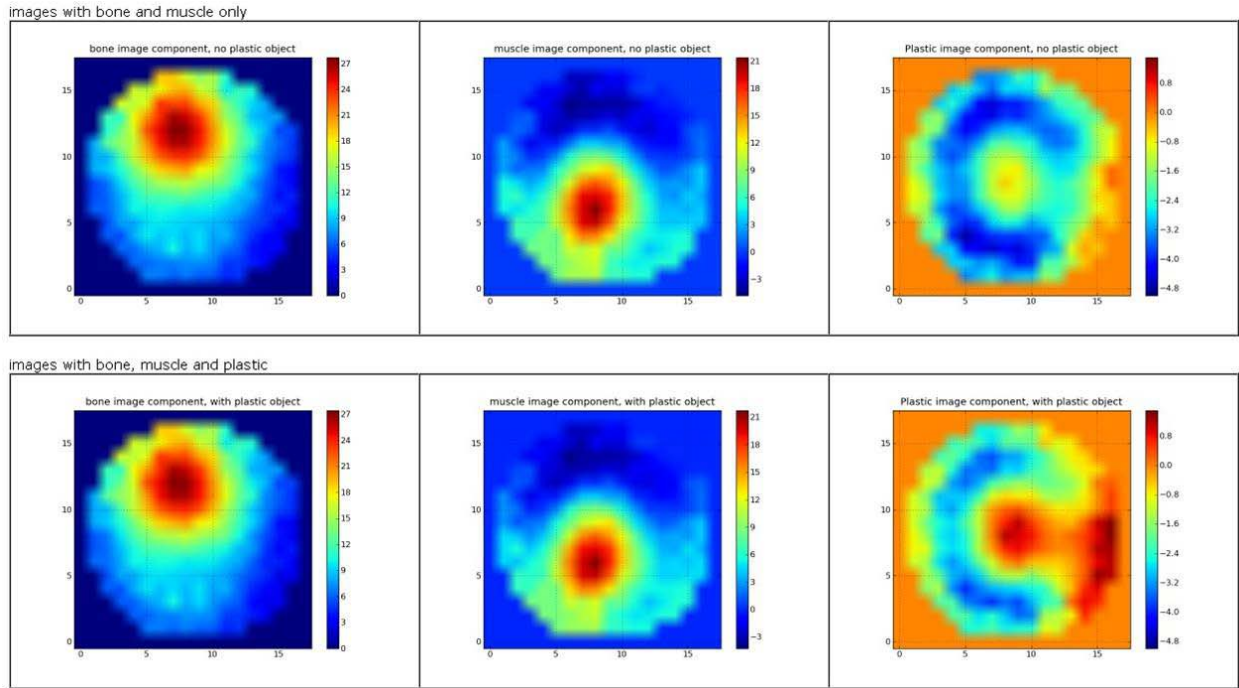


Figure ES-2. Single object images from linear decomposition of the composite multi frequency images. The top row is from bone and muscle simulations; the bottom row is from bone, muscle, and plastic simulations.

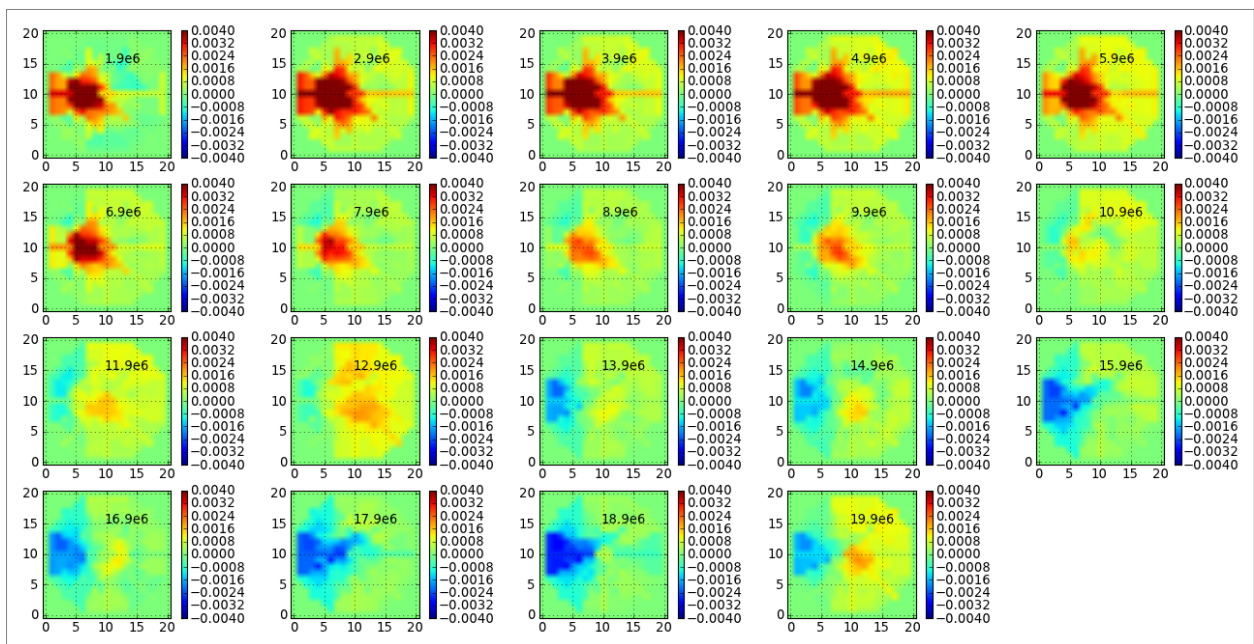


Figure ES-3. Images obtained at varying frequencies with the final laboratory prototype system.

3. Table of Contents

1. Abstract.....	2
2. Executive Summary.....	2
3. Table of Contents.....	5
4. List of Figures.....	5
5. Survey of correctional facilities.....	8
5.1. Contraband Items in the Corrections Environment.....	8
5.2. Smallest Object to be Detected.....	9
5.3. Operational Requirements.....	9
6. Feasibility study.....	10
6.1. Laboratory measurements.....	10
6.2. Detection limits.....	12
7. Image reconstruction.....	13
7.1. Back projection reconstruction.....	13
7.2. Multiple object discrimination.....	17
7.3. Summary of Image reconstruction of simulated data.....	17
8. Multi-frequency image decomposition.....	19
8.1. Initial FEM simulations at multiple frequencies.....	19
8.2. Linear modeling of multiple frequency images.....	20
8.3. Conclusions for multi-frequency image decomposition.....	26
9. Prototype development and experimental images.....	26
9.1. Experimental Images.....	32
10. Experimental multi-frequency images.....	37
11. Design of transceiver node system.....	42

4. List of Figures

Figure ES-1. Composite images at different frequencies.	3
Figure ES-2. Single object images from linear decomposition of the composite multi frequency images.	4
Figure ES-3. Images obtained at varying frequencies with the final laboratory prototype system.	4
Figure 1. Plastic object in DI water with shield and capacitive coupling nodes.	11
Figure 2. Photograph of experimental setup in air w/ metal tube and plastic tube filled with DI water.	11
Figure 3. ANSYS model: Cylindrical volume with saline water, 8 electrodes and cylindrical inclusion.	12
Figure 4. Voltage distribution in the model.	12
Figure 5. Projected variation of the maximum phase shifts with the radius of the insertion object.	13
Figure 6. Dipole field lines connecting the transmit node to each of the other receiver nodes.	14
Figure 7. Reconstructed image from line integral projection data with a 3 inch radius insertion object.	14
Figure 8. Reconstructed image from line integral projection data with a 1 inch radius insertion object.	15
Figure 9. Reconstructed images from FEM data with plastic insertion object in uniform saline solution.	16
Figure 10. Reconstructed images of a plastic insertion object placed in different positions.	16

Figure 11. Dielectric properties and object locations used for the three object FEM simulations.	18
Figure 12. Reconstructed images of single plastic insertion object, 2 body tissue objects and all 3objects.	18
Figure 13. FEM of 3 objects.	19
Figure 14. Image reconstructions of FEM simulations performed at 5, 10 and 20MHz.	20
Figure 15. Image of plastic object by scaling and subtracting the 5 MHz image from the 10 MHz image.	20
Figure 16. Linear model of composite multi frequency images from tissue and plastic objects.	21
Figure 17. Linear least square decomposition of the multi frequency composite images.	21
Figure 18. Path integral simulation images.	22
Figure 19. Object configuration for FEM simulations.	23
Figure 20. FEM simulated phase signal variations at the 17 receiver nodes for the 3 inclusion objects.	24
Figure 21. Composite images at different frequencies.	25
Figure 22. Single object images from linear decomposition of the composite multi frequency images.	25
Figure 23. 3D model of prototype EFT system with outer shield and capacitive sensor nodes.	27
Figure 24. Shield for prototype system with attached receiver board.	27
Figure 25. Inside the shield of the EFT system with transmit and receive nodes.	28
Figure 26. Circuit diagram for the receiver board.	28
Figure 27. Receiver PCB attached to system outer shield.	29
Figure 28. USRP data acquisition system.	29
Figure 29. Current lab prototype system configuration.	30
Figure 30. Relay diagram for acquisition of signals from 7 receiver sensor nodes and 1 transmit node.	31
Figure 31. GUI interface for a plotting application to monitor the signal phase in real time.	31
Figure 32. Sample placement s used in acquiring imaging data.	32
Figure 33. Sample placement at different radial offsets.	33
Figure 34. Phase profiles for simulated data.	34
Figure 35. Phase profiles for experimental data.	34
Figure 36. Reconstructed images from simulated and experimental data.	35
Figure 37. Reconstructed images from simulated and experimental data.	36
Figure 38. Images from simulated data with 16 and 8 nodes.	36
Figure 39. EFT system node arrangement and numbering.	38
Figure 40. Phase modulations observed during frequency sweeps.	38
Figure 41. Phase standard deviation with initial configuration with Tx output power of 4 dBm.	39
Figure 42. Phase standard deviation with output power of 10dBm.	39
Figure 43. EFT system being tested with additional shielding.	40
Figure 44. Receiver output measured on a spectrum analyzer with and without additional shielding.	40
Figure 45. Images obtained at varying frequencies without additional shielding.	41
Figure 46. Images obtained at varying frequencies with additional shielding.	41
Figure 47. Study schematic of an advanced charge amplifier circuit topology.	43

Figure 48. EFT system diagram with transceiver nodes.	45
Figure 49. Transceiver layout (component side).	46
Figure 50. Transceiver top layer board mask.	47
Figure 51. Transceiver ground layer board mask.	48
Figure 52. Transceiver third layer board mask.	49
Figure 53. Transceiver bottom (fourth) layer board mask.	50
Figure 54. Transceiver board component layout silk screen.	51
Figure 55. Relay board layout (component side).	52
Figure 56. Relay board masks.	53

5. Survey of correctional facilities

From discussions with the California Department of Corrections, Folsom State Prison, and participants at the 2008 Conference of the Western States Corrections Association, informal surveys were compiled. The following section presents a summary from those surveys.

5.1. *Contraband Items in the Corrections Environment*

The following table lists major categories of contraband, along with examples of each category.

Category	Examples
Metallic weapons or weapon parts; metal pieces that can be sharpened into weapons	.22 (~5.6 mm) caliber bullet (single or multiple)
	Razor blade (single or multiple)
	Hacksaw blade
	Knife or shank
	Small handgun
Plastic or wooden objects that can be sharpened into weapons	Anything the size of a toothbrush handle (~8 mm diameter by 10 cm long) or larger
Handcuff keys	Steel handcuff keys (<2 mm diameter by ~1 cm long)
	Plastic tabs from insulin self-test kits, usable as handcuff keys (<2 mm diameter by ~1 cm long)
Electronics	Wireless communication devices: cell phones, personal digital assistants
	Battery chargers for wireless devices
	SIM cards for cell phones
Financial instruments	Cash (paper currency)
	Credit cards
Documents	Driver's licenses or other photo ID
Cosmetics	Lipstick
	Eye shadow, eye liner
	Lotions, gels
Recreational substances	Tobacco (loose and in cigarettes)
	Marijuana
	Cocaine and other hard drugs
Drug paraphernalia	Hypodermic needles
	Cigarette papers
	Matches
	Cigarette lighters
Other metallic items	Jewelry

The list can evolve over time as legislation, technology, and inmate preferences change, so the table is not exhaustive. In effect, contraband consists of *anything* other than naturally occurring substances or legitimate personal hygiene products (e.g., tampons) in a body cavity. Most of the items in the table have been observed to be smuggled in lower body cavities.

5.2. ***Smallest Object to be Detected***

It is desired to detect all objects listed in the Table above. However, it is recognized that the smallest ones (the plastic handcuff key, the SIM card, etc.) may not be detectable. Since at the moment, no non-invasive technology is available for body cavity inspection, we have been told that we should concentrate on the possible, and it will be an improvement on the current state of the art.

Detectability is a function of the contrast in dielectric constant between the object and surrounding tissue. Accordingly, I propose the following detection goals for the present development effort.

Material	Detection Goal
Nonferrous metal	.22 caliber bullet
Ferrous steel	Single razor blade
Plastic	Cylinder 8 mm in diameter by 10 cm long

5.3. ***Operational Requirements***

1. **Contacting vs Non-contacting**

A non-contacting system, and one that allows the subject to remain clothed, is strongly desired. However, a system based on electrode contact is not ruled out completely, although the resulting market for the device would be smaller. A non-contacting system could be used not only on inmates, but also on visitors and corrections officers. A system requiring direct skin contact would likely not be applicable to non-inmates.

Accordingly, the design goal is a non-contacting (i.e., capacitively coupled) system. Only if the model calculations indicate that detection goals cannot be met with a non-contacting system will a contacting (electrode-coupled) system design be considered, and then only after a follow-up set of interviews with Corrections officials.

Two issues to consider are the effects of subject movement while being screened, and variations in subject cross sectional area. Motion artifacts would be intrinsically minimized by an electrode-coupled system; the design should include concepts to mitigate noise from lateral subject motion in a capacitively coupled system.

2. **System size: subject girth**

A key issue is the effect of variations in subject girth. The system should accommodate individuals up to the 95th percentile in girth. The system's detection performance should be minimally affected by differences in girth.

3. Overall system footprint and weight

Compact, lightweight systems are strongly desired. It is desired to be able to stow the system (e.g., in a closet) when not in use. Accordingly, the design goal is a system whose ground footprint expands minimally on the size of the subject.

Concerns that a system light enough to move might itself be used as a weapon by an inmate are discounted: the system could be affixed to a floor or wall during operation. Thus, a system light enough to be moved by one person is preferred to a heavier one.

4. System cost

State Corrections budgets vary widely in absolute terms and in terms of dollars spent per inmate. In states such as California, the Corrections budget is the largest single line item. The budget is dominated by operating expenses and salaries, with new construction second. Despite the disparity in per-capita spending, all corrections budgets are very lean on equipment. Low price points are essential for sales into this market. In discussions with corrections officials, we have learned that the average price paid for conventional metal detection portals is about \$6,000 per unit, and our contacts have said that they would consider that a reasonable price for a non-invasive body cavity screening system.

5. Ease of use

The system must be simple to operate, and results must be presented in unambiguous, intuitively understandable form. Having an image or map of dielectric constant distribution available as a backup would be nice, but is not required. Wired or wireless communication to a central control node is desired.

6. Throughput

No strong opinion was expressed on the importance of high throughput; a time span of a few tens of seconds for data collection and analysis is perfectly adequate.

6. Feasibility study

During the feasibility phase of the project, we explored with both experiments and simulations the range of phase shifts expected for foreign objects and tissue samples (simulated with saline solution phantoms) and whether such phase shifts were detectable with our receiver designs.

6.1. Laboratory measurements

Several bench-top experimental systems were setup to test the phase sensitivity of different objects and backgrounds with different methods of coupling. Figure 1 and Figure 2 show two such setups with capacitive and inductive coupling to the samples. These measurements were also useful for checking the results from the Ansys finite element modeling (FEM) simulations (Figure 3 and Figure 4) and giving a rough estimate of the sensitivity needed for the prototype system. Details of the laboratory measurement results were presented in the progress reports. The overall summary, however, was that non-tomography measurements based on simple multi-node systems shown in Figure 1 and Figure 2 are not capable of discriminating plastic objects from the phase scatter of saline solutions matching conductivities of different human tissue.

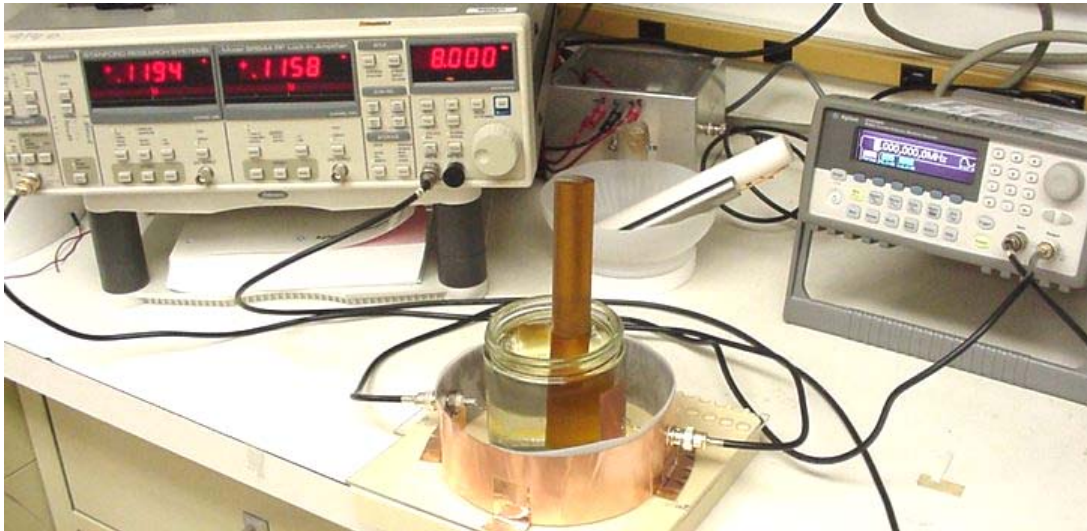


Figure 47. Plastic object in DI water with shield and capacitive coupling nodes.

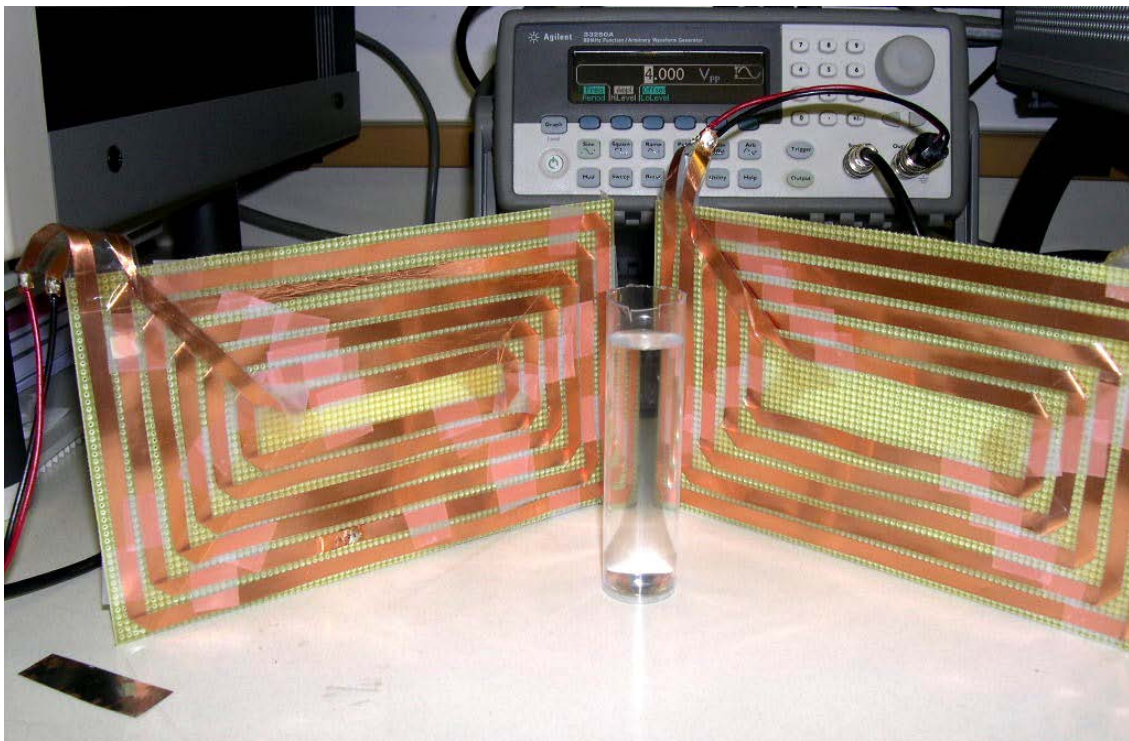


Figure 48. Photograph of experimental setup in air w/ metal tube and plastic tube filled with DI water.

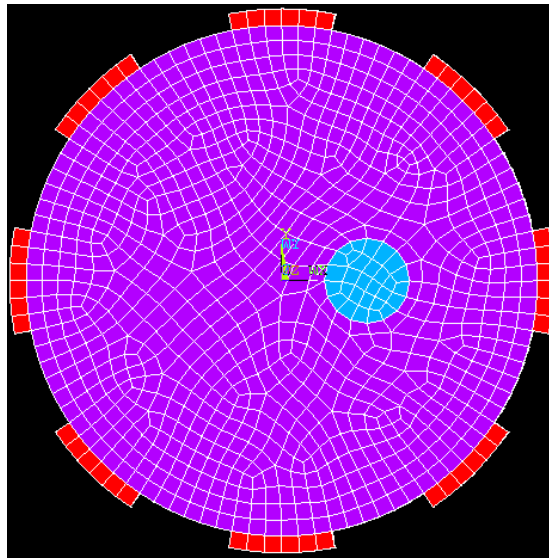


Figure 49. ANSYS model: Cylindrical volume with saline water, 8 electrodes and cylindrical inclusion.

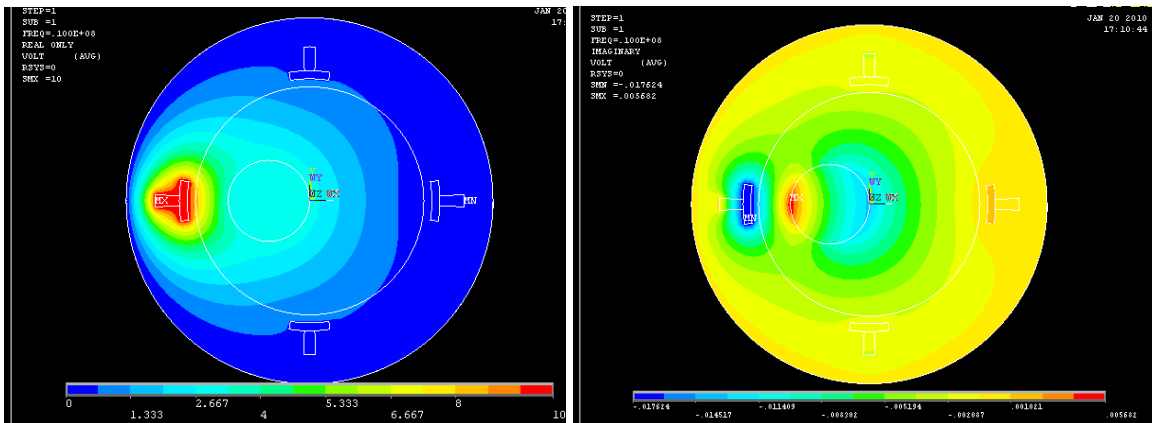


Figure 50. Voltage distribution in the model. Excitation frequency - 10 MHz; inclusion size – 50 mm (2”); Real component of electric potential (LHS); Imaginary component of electric potential (RHS).

6.2. Detection limits

The size limitations in detectable plastic objects were examined plotting the maximum phase shift signal detected with plastic insertion objects of different sizes. The phase shift due to the insertion object should vary with the cross sectional area of the object. Figure 5 shows a fit to the maximum signal phase shifts obtained from FEM simulations to a quadratic curve with varying radii. The curve indicates that detection of objects below 0.5 inch radius would require a phase stability of the order of 100 micro-radians. As discussed in the prototype development section, the initial measurements of electronic phase stability of the prototype system indicate that the electronic stability is well within this limit.

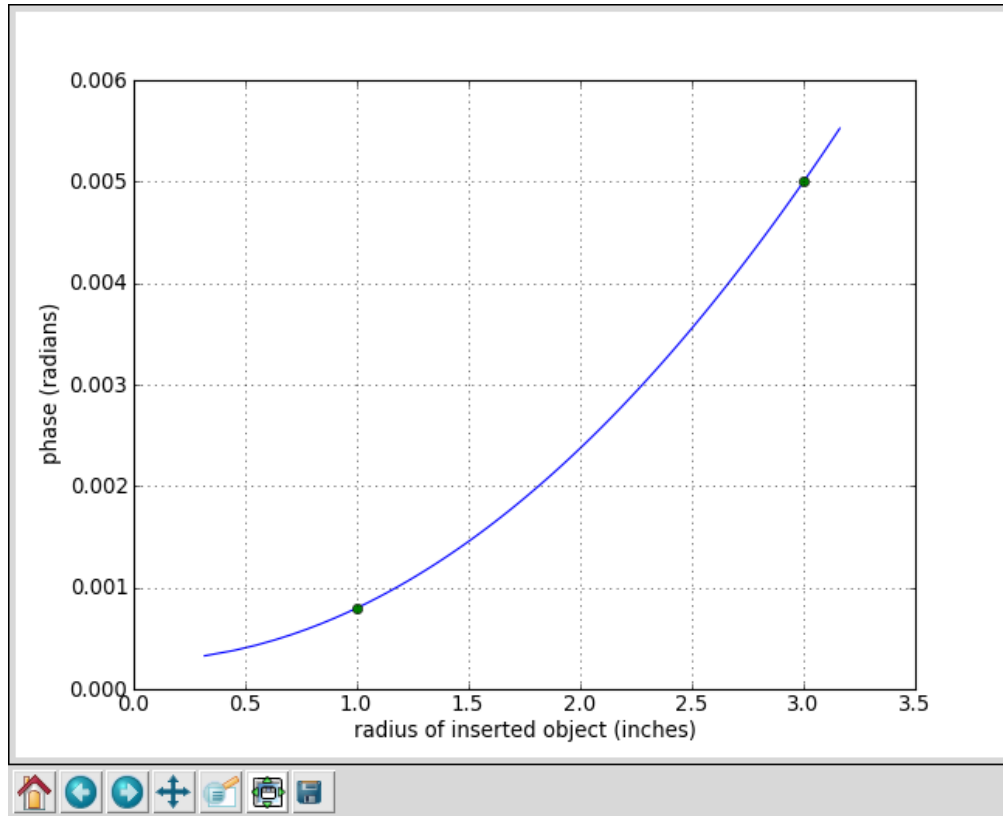


Figure 51. Projected variation of the maximum phase shifts with the radius of the insertion object. The two green dots represent phase shifts that were measured from FEM simulations.

7. Image reconstruction

Image reconstruction algorithms based on back projection methods were written and tested initially with simulated data. The reconstruction algorithm was tested with simulated projections from field line integrals as well as Ansys finite element modeling (FEM) data. The results show that a strong convolution filtering in the reconstructed image results from the electromagnetic interactions within the system that limit the overall resolution of the image. Despite the poor resolution quality of the images from FEM simulations, the images indicate that electric field tomography (EFT) is still able to act as a detector of anomalies within human tissue background.

7.1. Back projection reconstruction

Back projection reconstruction methods are standard algorithms used in x-ray computer tomography (CT) for medical imaging applications. The problem further complicated in EFT because the projections occur along the electric field lines which are curved rather than straight as in x-ray CT.

The image below shows a typical electric field line and projection scenario for EFT. The 17 red dots represent sensor nodes. The node at the bottom position acts as the transmitter while the other nodes act receivers. The figure shows dipole field lines from the transmit node to each of the receiver nodes. The circular figure placed inside the node ring represents the insertion object

being imaged. The panel in the figure labeled “projection” shows the projection “signal” form the insertion object obtained at the 16 receiver nodes from line integrals along curved field lines. A similar set of projection profiles are then obtained by shifting the transmit node to adjacent nodes in the circle until a full set of 17 projection profiles are obtained. Figure 7 and Figure 8 below show the images reconstructed using curved field line back-projection. In both cases the sensor ring had a radius of 10 inches. Figure 7 shows the reconstructed image for an insertion object of 3 inch radius; and Figure 8 shows the image for a 1 inch radius object.

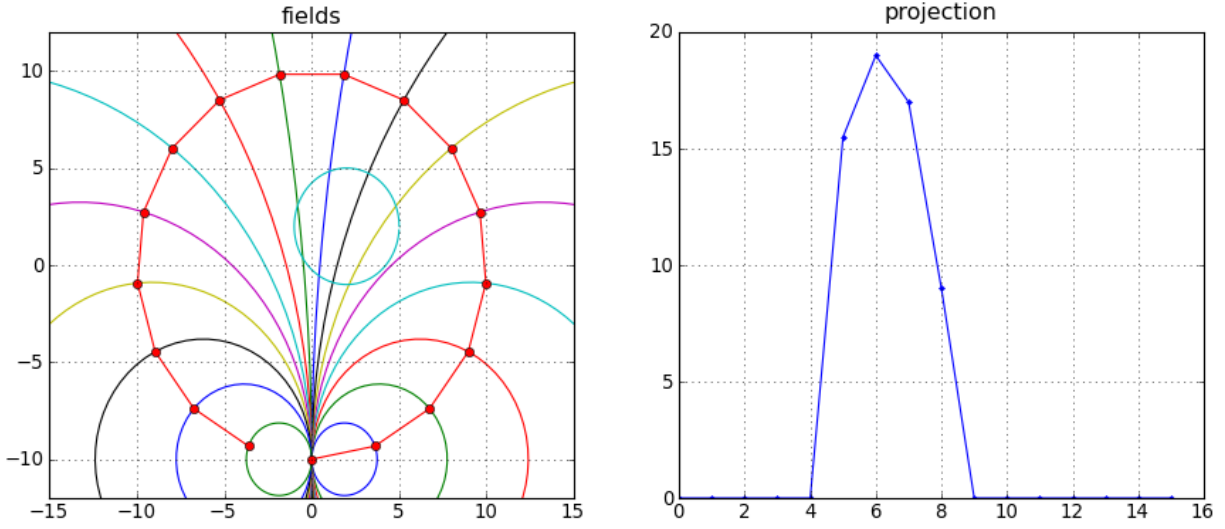


Figure 52. Dipole field lines connecting the transmit node at the bottom position to each of the other receiver nodes. The projection profile shows the line integral projection along each of the field lines at the 16 receiver nodes due to the circular inserted object.

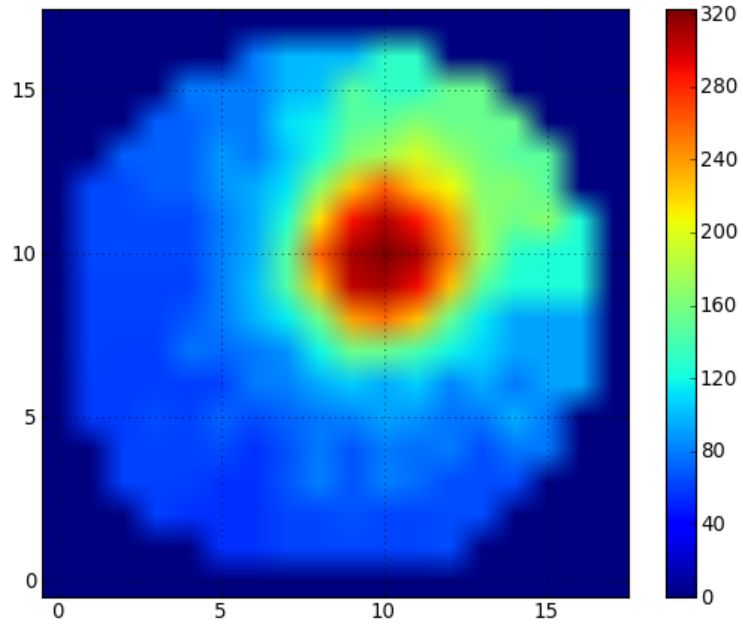


Figure 53. Reconstructed image from line integral projection data with a 3 inch radius insertion object.

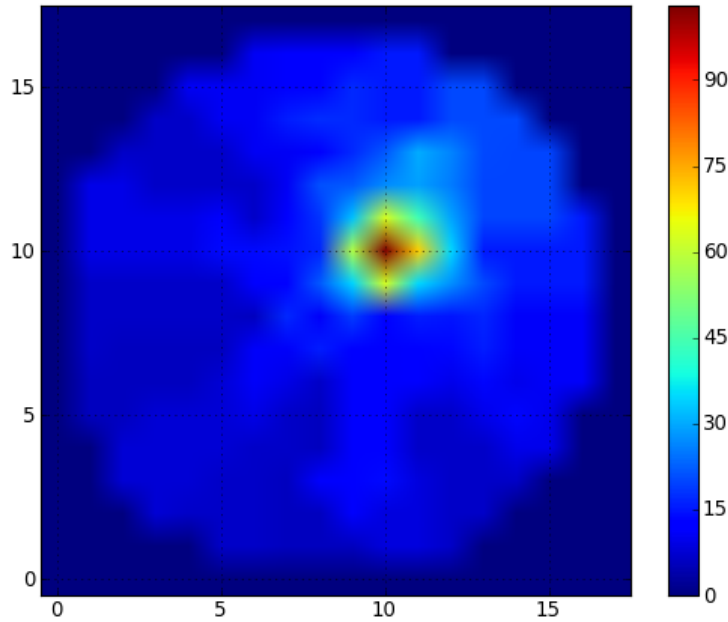


Figure 54. Reconstructed image from line integral projection data with a 1 inch radius insertion object.

The same reconstruction algorithm was then used on data from FEM simulations for similar systems. The resulting images are shown in Figure 9, below. The FEM was performed on a 2D system where a plastic object was placed inside a uniform saline solution background. The insertion object was placed along the x axis with a 1 radius offset from center. The signal that was used for the reconstruction is the phase shift of the detected signal with respect to the transmit signal. The images show the correct displacement shift of the object along the x axis; however, a strong broadening effect is seen so that difference between the 1 and 3 inch radii objects are difficult to see from the shape of the image alone. This is in stark contrast to the images obtained from simulated line integral projections shown in Figure 7 and Figure 8. We believe this image broadening when electromagnetic interactions are taken into account in FEM is due to the fact that the image reconstruction assumes the field lines are not perturbed by the insertion object. FEM, however, shows strong perturbations of the field lines due to the insertion objects.

Figure 10 below shows reconstructed images from FEM data with the insertion object placed in different orientations and positions. The images show that the phase shift signal due to the plastic insertion object can change by up to a factor of 2 in magnitude depending on the location of the object, with closer proximity to the nodes resulting in larger signal.

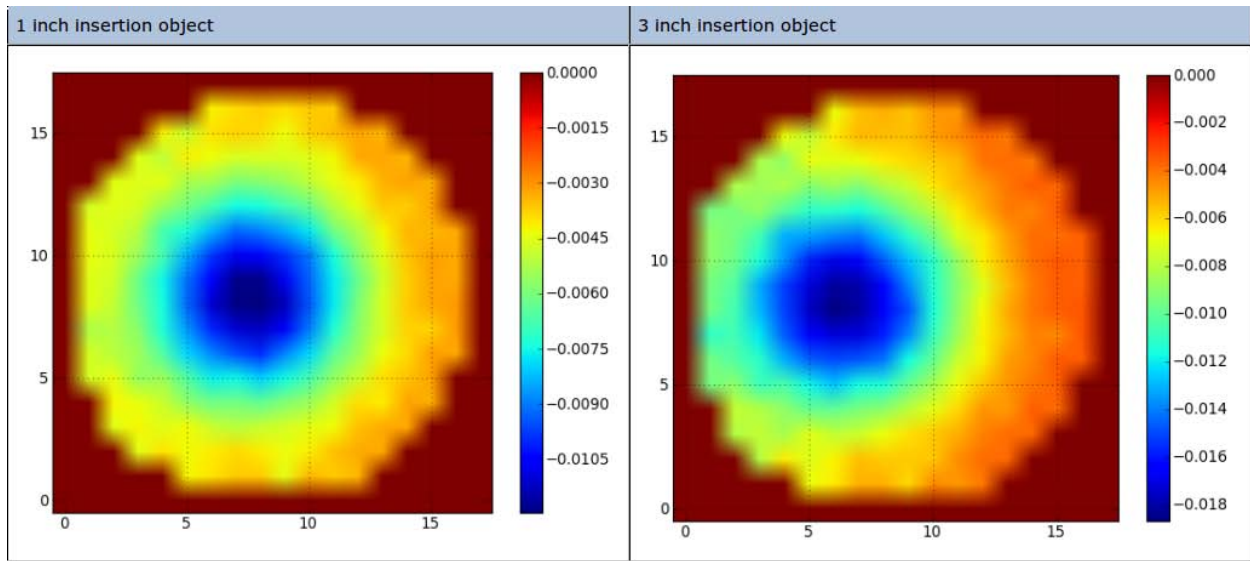


Figure 55. Reconstructed images from FEM data with a plastic insertion object in a uniform saline solution background. The objects of different radii were displaced by their respective radii along the x axis.

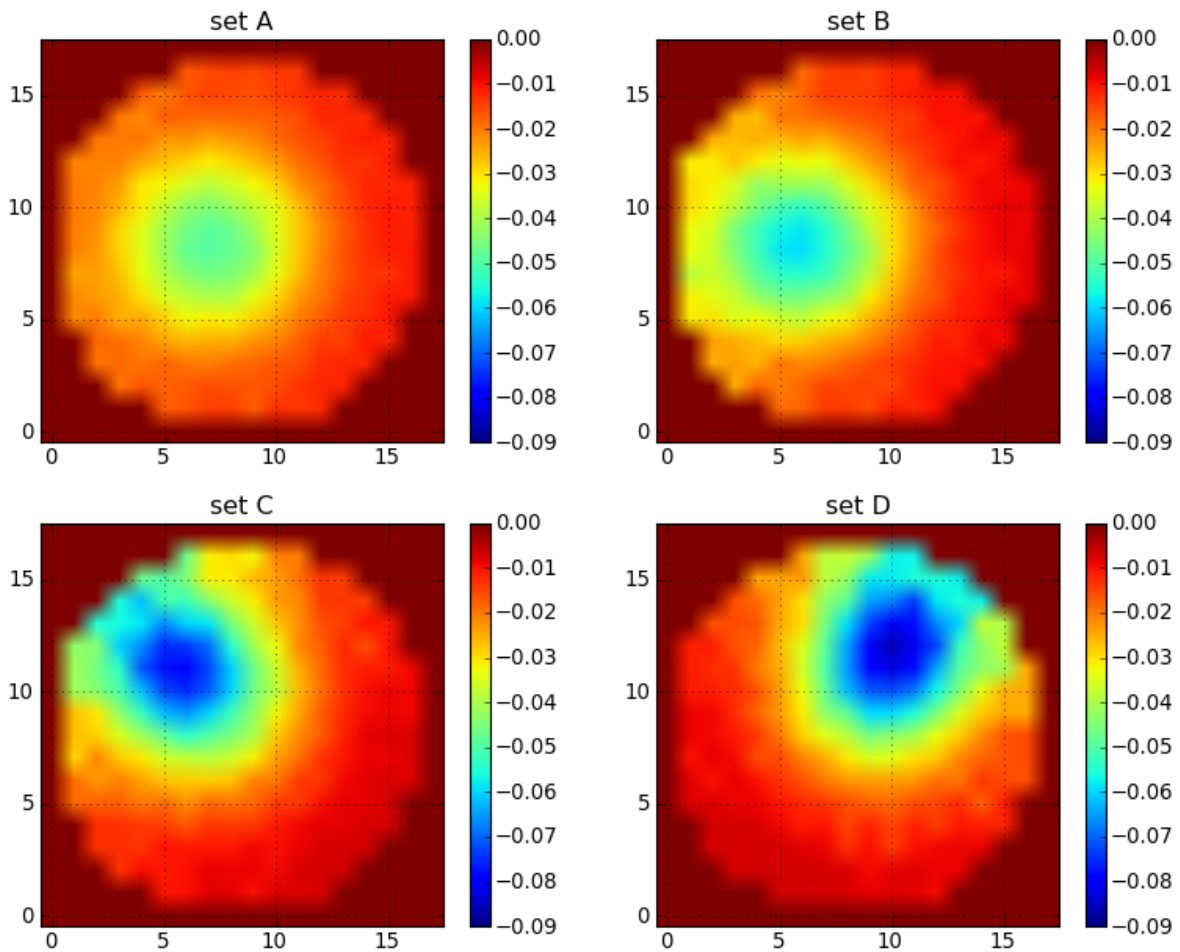


Figure 56. Reconstructed images of a plastic insertion object placed in different positions. All images here use the same color scaling for the image intensity.

7.2. Multiple object discrimination

The previous examples all involved imaging a single object in a uniform background. The detection of anomalous objects within body cavities involves, however, detection of objects within non uniform tissue background with varying electrical properties. The initial attempt at quantifying detectability of plastic objects in a non uniform background is shown in the figures below. Figure 11 shows the Ansys model configuration used for the FEM simulations. Objects 2 and 3 represent differing body organs with variations in both permittivity and conductivity. Object 1 represents the smaller plastic object with much lower conductivity and permittivity.

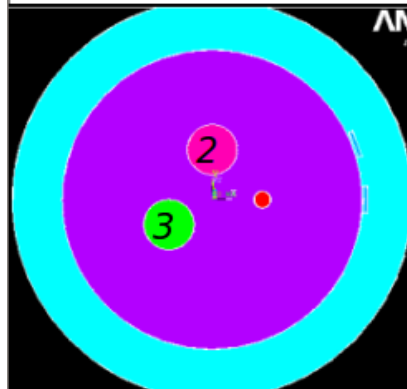
The resulting reconstructed images are shown in Figure 12. The image for just objects 2 and 3 show that due to low resolution, the separate objects are not seen, and just a single elliptical image is obtained. When all 3 objects are included in the simulations, a clear distortion of the elliptical image is seen however because objects 2 and 3 were larger and thus dominate the phase signal, the location and shape of object 1 is difficult to see. However, even though the phase magnitude from object 1 is much smaller than those due to objects 2 and 3, it is clearly distinguished in that the object 1 causes a negative signal phase shift with respect to the saline background while objects 2 and 3 causes a positive relative phase shift. The phase shift due to object 1 was of the order of 500 micro-radians which, as discussed below, is far above the stability of the system electronics. Thus even though it is difficult to see the plastic object in the 3 object image, the plastic would have easily been detected with a simple threshold detector. The simple lab measurements discussed in the previous section and in progress reports indicate that the plastic object in the 3 object system shown in Figure 11 would not have been detectable without some level of spatial separation of the signal given by EFT.

Although for this particular example, the images with and without the plastic inclusion object was distinguishable, the detection of the plastic object would not be as easy for other configurations of the inclusion objects or for cases where the background variations were more complicated than just two tissue-like objects. Iterative reconstruction methods such as algebraic reconstruction techniques may improve the overall resolution of the images, however, despite active research in the field, low frequency electro-magnetic tomography (sometimes referred to as “soft” tomography) methods such as EFT generally cannot approach the resolution and image quality of X-ray CT or magnetic resonance imaging.

7.3. Summary of Image reconstruction of simulated data

A simple back-projection along curved field lines algorithm was implemented to reconstruct the EFT data obtained from FEM simulations. The reconstructed images from FEM data showed significant broadening that is not seen with simulated data of line integral projections. We currently believe this is mainly due to perturbations of field line from the electromagnetic interactions with insertion objects. Despite the poor resolution of EFT, it was shown that the spatial separation provided by EFT allows detection of plastic objects in tissue background that would not have been possible with non-tomography methods. The conclusion however is that the spatial separation provided by EFT is not enough for the need of a body cavity scanner.

Input parameters for simulations:				
	Diam.	Pos.	ϵ	σ , [S/m]
Air/Ground	24"	(0,0)	1	1.00E-10
Body:	18"	(0,0)	80	0.08
Inclusion 1:	1"	3" at 0 deg	4	1.00E-10
Inclusion 2:	3"	3" at 90 de	100	0.10
Inclusion 3:	3"	3" at 210 d	150	0.05
Electrode:	10 deg	Freq. [MHz]	10	



July 19, 2010

3 inclusions in 24" set

Figure 57. Dielectric properties and object locations used for the three object FEM simulations.

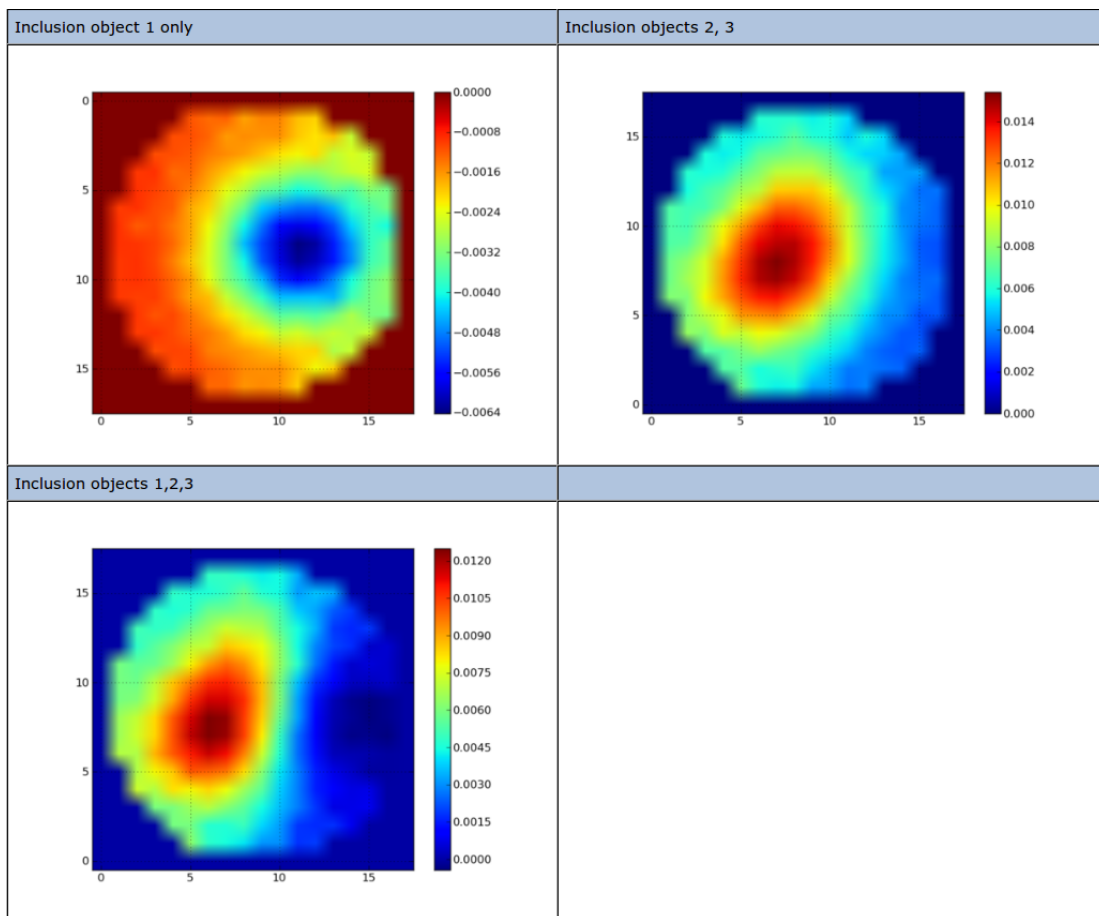


Figure 58. Reconstructed images of a single plastic insertion object (object 1), two body tissue insertion objects (object 2 and 3) and all three objects.

8. Multi-frequency image decomposition

Due to the inherent poor resolution of the electric field tomography (EFT) images, FEM simulations and image reconstruction methods were examined using irradiation frequencies ranging from 1 to 20 MHz.

8.1. Initial FEM simulations at multiple frequencies

Figure 13 shows the objects used in the FEM simulations. Two identical 3 inch objects with “tissue-like” electrical properties were placed in the imaging system with a smaller 1 inch diameter plastic object. The images reconstructed from the FEM simulations done at 5, 10 and 20 MHz are shown in Figure 14. The top row shows the images from simulations of just the 2 tissue objects and the bottom row shows images reconstructed from simulations from all 3 objects. In the previous section, we showed an image from a similar 3 object simulation where the plastic object was detectable from image region where the image intensity became negative. Similar distortion of the image can be seen in the 3 object image at 10MHz. The distortion and difference between the 2 object and 3 object images become less pronounced at 20MHz. The image set at 5MHz shows the largest difference between the 2 object and 3 object images, however since at this frequency, it appears the both the plastic object and the tissue objects show the same signal phase, and thus, the same sign in the image intensity, it becomes more problematic in detecting the presence of the plastic object in the 5 MHz image.

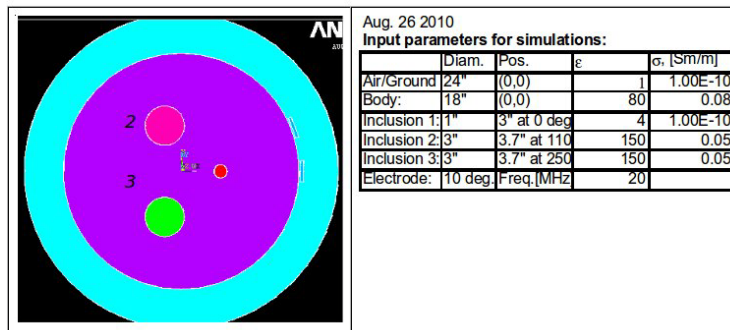


Figure 59. FEM of 3 objects. Objects 2, 3 with diameters of 3 inches had “tissue like” electrical properties, and the smaller 1 inch object had electrical properties of a generic plastic material.

Despite the observation from these imaging results that no image obtained at any one frequency would lead to distinctly better detection of the foreign plastic object in a tissue background, the series of images at the three frequencies shows clear differences in the trends in the image intensities as functions of the irradiation frequency. This indicates that there may be a way to cancel out the tissue background leaving the image of just the plastic by acquiring the EFT signals at multiple frequencies. In this particular example, by simply scaling the 5MHz image by a factor 4 and subtracting it from the 10 MHz image, an image of just the plastic object alone can be obtained as shown in Figure 15.

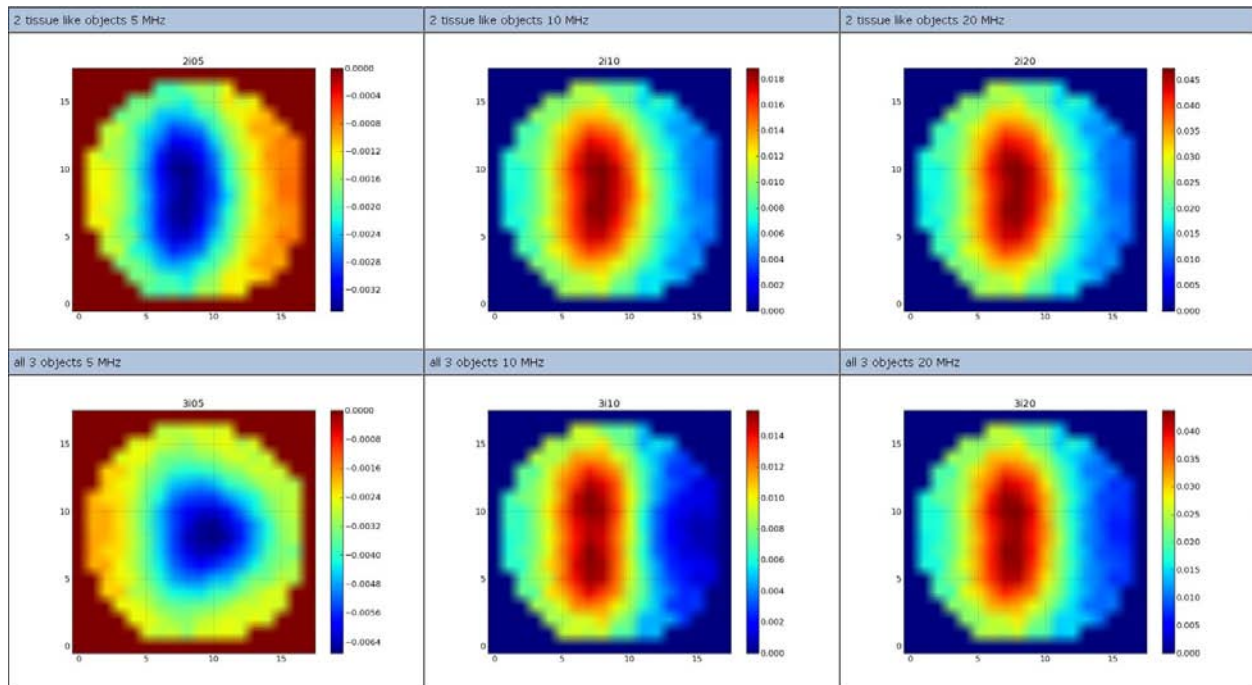


Figure 60. Image reconstructions of FEM simulations performed at 5, 10 and 20MHz. The top row are from simulations of just the 2 tissue-like objects; the bottom row are from simulations of all 3 objects.

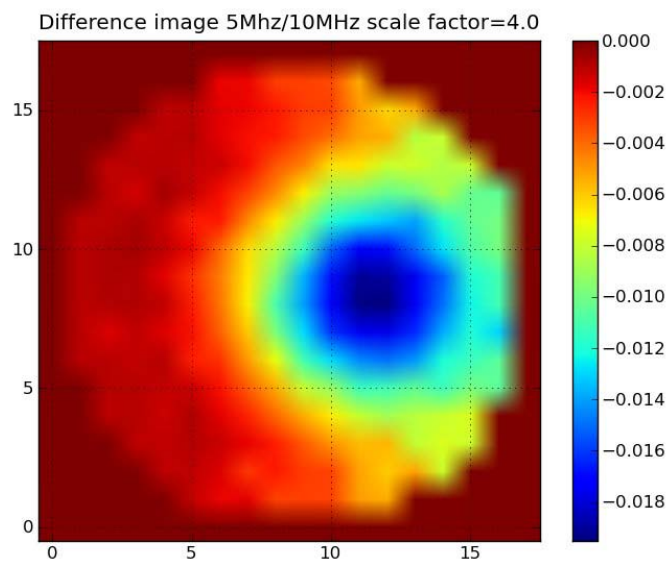


Figure 61. Image of the plastic object obtained by subtracting the 5 MHz image from the 10 MHz image with a scaling factor.

8.2. Linear modeling of multiple frequency images

In the previous section, we showed the ability of using the difference in phase response of tissue and plastic objects to cancel out the tissue image leaving only the image from the plastic. The previous example, however, showed separation of the plastic object from as single tissue object

using a single scaling factor. It is clear that when there are multiple tissue-like objects that behave differently under irradiation at varying frequencies, a single parameter is no longer enough to cancel out the images from the tissue background. If however, there is a clear enough distinction between the multi-frequency phase response of the plastic and other tissue objects, decomposition of the plastic image may still be achieved through modeling the full composite image.

We started examination of the image decomposition with simple linear models. Figure 16 shows one such linear model. The vector \mathbf{b} is composed of the acquired (or simulated) multi frequency composite images, and the vector \mathbf{x} is composed of pure single component images of two different tissue objects, $T1$ and $T2$ and a plastic object. The model assumes the composite images at each frequency are linear superpositions of single component images, with the superposition scaling factors forming the matrix \mathbf{A} . The model further assumes the intensity of the plastic object is constant at all frequencies, however, this is not a requirement for the linear decomposition method being examined; the only requirement is that all the elements of the coefficient matrix \mathbf{A} be known through experiments or simulations. Once the coefficients are known, and the images at the multiple frequencies have been obtained, the matrix equation can be inverted as shown in Figure 17 to obtain the vector of decomposed images stored in \mathbf{x} . The requirement in the matrix inversion process is that the number composite images acquired at different frequencies be larger than the number of pure image objects. With this condition, the matrix inversion shown in Figure 17 gives the best solution for the image decomposition in the “least square sense”.

$$\begin{array}{c}
 \begin{bmatrix} 1 & C_{\nu_1}^1 & C_{\nu_1}^2 \\ 1 & C_{\nu_2}^1 & C_{\nu_2}^2 \\ \vdots & \vdots & \vdots \\ 1 & C_{\nu_j}^1 & C_{\nu_j}^2 \end{bmatrix} \begin{bmatrix} I_p \\ I_{T1} \\ I_{T2} \end{bmatrix} = \begin{bmatrix} M_{\nu_1} \\ M_{\nu_2} \\ \vdots \\ M_{\nu_j} \end{bmatrix} \rightarrow \mathbf{Ax} = \mathbf{b} \\
 \begin{array}{l} \uparrow \\ \text{Image scaling factors} \\ \text{at varying frequencies} \end{array} \quad \begin{array}{l} \uparrow \\ \text{Tissue images} \end{array} \quad \begin{array}{l} \uparrow \\ \text{Acquired images} \end{array} \\
 \end{array}$$

Figure 62. Linear model of composite multi frequency images from tissue and plastic objects.

$$\begin{array}{c}
 \mathbf{Ax} = \mathbf{b} \\
 \mathbf{x} = \underbrace{(\mathbf{A}^T \mathbf{A})^{-1} \mathbf{A}^T}_{\text{Acquired images}} \mathbf{b} \\
 \begin{bmatrix} a_{1,\nu_1} & a_{1,\nu_2} & \dots & a_{1,\nu_j} \\ a_{2,\nu_1} & a_{2,\nu_2} & \dots & a_{2,\nu_j} \\ a_{3,\nu_1} & a_{3,\nu_2} & \dots & a_{3,\nu_j} \end{bmatrix} \begin{array}{l} \leftarrow \text{Selects } I_p \\ \leftarrow \text{Selects } I_{T1} \\ \leftarrow \text{Selects } I_{T2} \end{array}
 \end{array}$$

Figure 63. Linear least square decomposition of the multi frequency composite images.

Figure 18 shows the results of the linear image decomposition method for images constructed from path integral simulation data. As discussed in the previous reports, these simulations assume that the signal phase obtained at each sensor node is due to path integrals of the phase shift along undistorted electric field lines. The scaling coefficients were put into the model as exact numerical scale factors in the path integration. The top row of Figure 18 shows composite images at 3 of the frequencies used in the decomposition. The second row shows the linear – least square decomposed images obtained by inverting the scaling coefficient matrix for the 3 objects (with 1”, 3”, and 4” diameters). With the assumptions used in the simulations, the image decomposition is exact, and the decomposed images are identical to the images that would have been obtained for the pure single object alone.

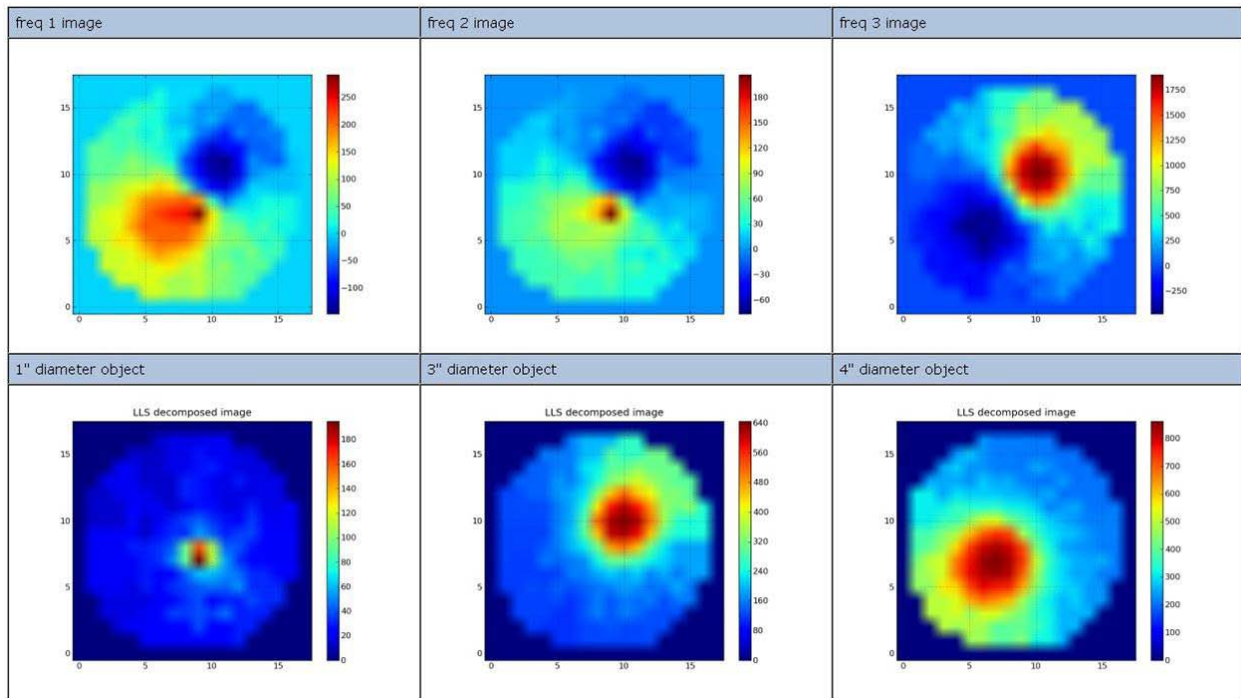


Figure 64. Path integral simulation images. The top row shows the composite images at 3 frequencies. The bottom row shows the decomposed object images.

Next, we tested the image decomposition method with data from FEM simulations. Figure 19 shows the three objects used in the simulations. The circle labeled 2 represents bone and used the (conductivity, permittivity) pair of (0.2 S/m, 60), and a 3 inch diameter; the circle labeled 3 represents muscle and used (0.6 S/m, 150) and the same 3 inch diameter; the smaller circle represents plastic and used (10e-10 S/m, 4) with a 1 inch diameter.

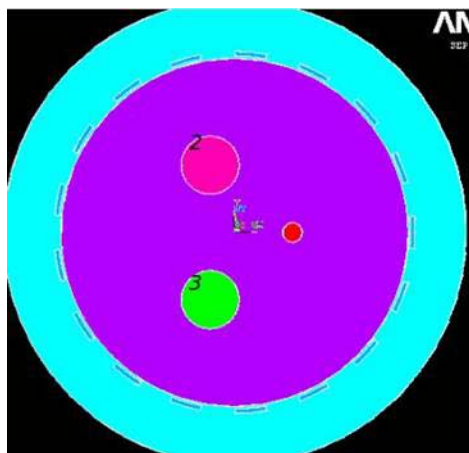


Figure 65. Object configuration for FEM simulations.

With FEM simulations, it was no longer possible to set the scaling factor coefficients into the simulations but had to be obtained from simulation results in the same manner we anticipate obtaining them in experiments. A separate set of non-imaging simulations were performed where objects with the same electrical properties as described above but now all objects with the same diameter of 3 inches were placed one at a time at the center of the imaging system. A set of phase signals were then obtained using just one node as the transmitter and the remaining 17 nodes as receivers. The phase signals detected at multiple frequencies are shown in Figure 20. As we had hoped, the simulation showed that the variation of the signal phase at the different irradiation frequencies were distinctly different for the 3 objects examined. The phase value at receiver node number 8 for all the difference frequencies was used to construct the scaling coefficient matrix.

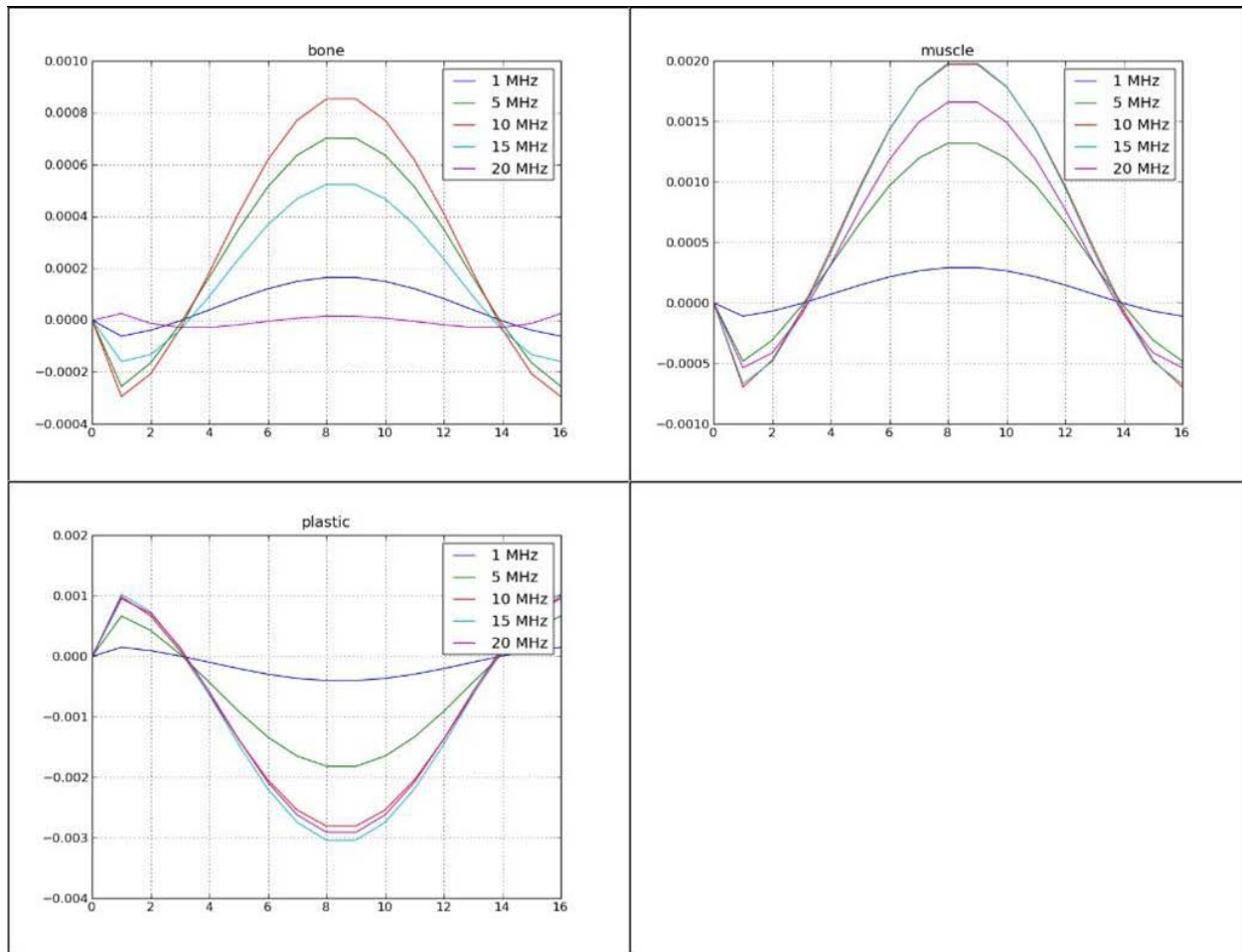
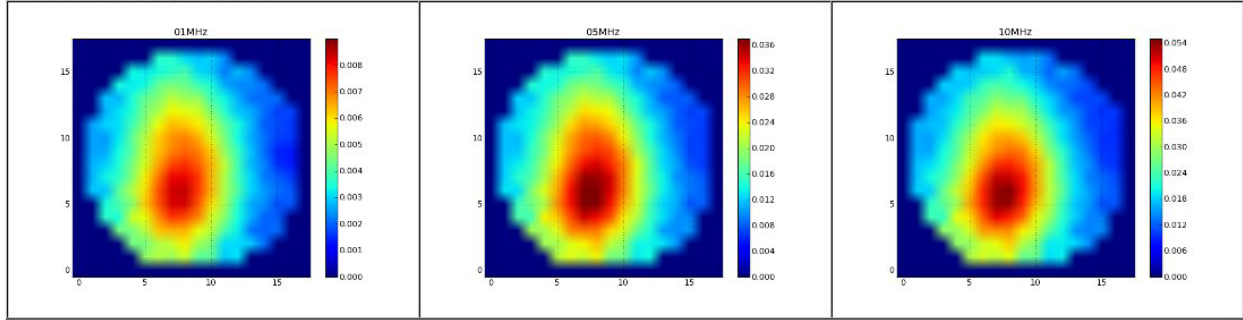


Figure 66. FEM simulated phase signal variations (in radians) at the 17 receiver nodes for the 3 inclusion objects.

FEM simulations were then run using the configuration of objects shown in Figure 19 at 1, 5, 10, 15 and 20 MHz. Two sets of multi frequency simulations were run, first with only the two tissue like objects and then with all three objects including the plastic. Figure 21 shows the reconstructed composite images at 1, 5, and 10MHz (similar trends are seen at 15 and 20 MHz as well). The color scaling is the same for the 2 and 3 object images at each frequency. Although an amplitude modulation is introduced by the insertion of the plastic object, no qualitative change in the image can be observed between the 2 and 3 object images at any given frequency. We conclude from these results that it would not be possible to detect for the presence of the plastic object at any one given frequency.

Figure 22 shows the decomposed images into bone, muscle and plastic image components. The top row shows the results from the two object simulated data (no plastic inclusion); the bottom row shows the images from three object simulations which includes the plastic object. For each of the component images for the 2 and 3 object simulations, the color intensity axis is kept constant. Both the bone and muscle images for the 2 and 3 object simulations appear almost identical. In the case of the plastic component, however, a clear difference in the image can be detected for the case the plastic object is included in the simulations.

Bone and muscle only, no plastic



Bone, muscle and plastic

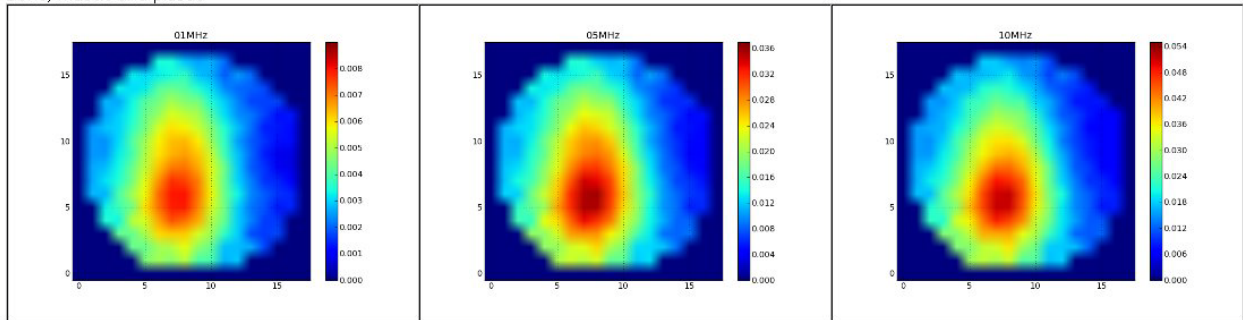
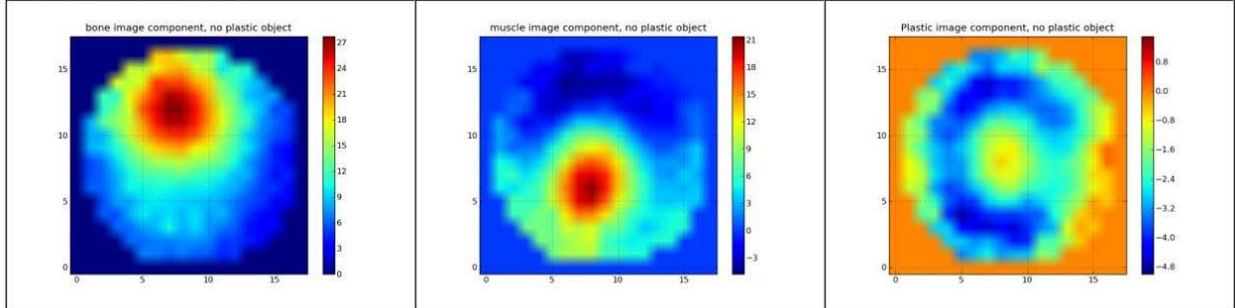


Figure 67. Composite images at different frequencies. Top row images are from bone and muscle simulations. Bottom row images are from bone, muscle, plastic simulations.

images with bone and muscle only



images with bone, muscle and plastic

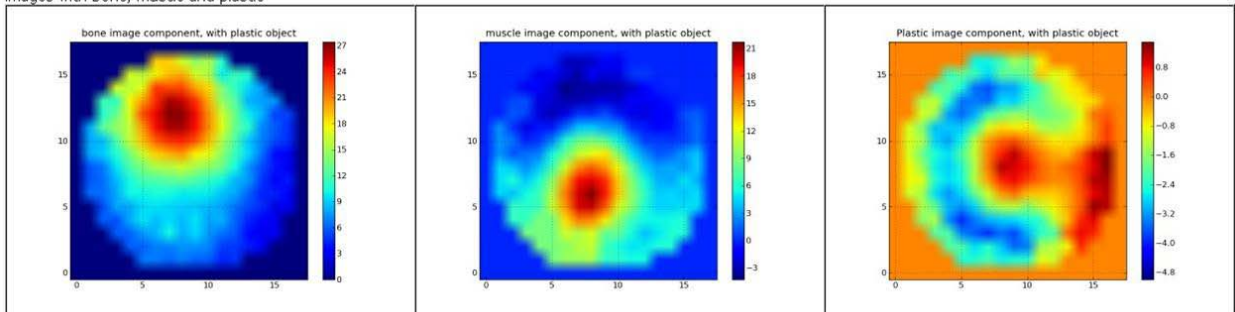


Figure 68. Single object images from linear decomposition of the composite multi frequency images. The top row is from bone and muscle simulations; the bottom row is from bone, muscle, and plastic simulations.

8.3. Conclusions for multi-frequency image decomposition

We have shown based on FEM simulations that linear modeling multi-frequency multi-object images can be used to decompose the composite images into single object images allowing for detection of plastic insertion objects within human tissue clutter that would not have been possible in the original composite images. The method shows promise for the use of EFT as a detector for the presence of foreign objects within a nonuniform body tissue background despite the inherent low resolution of EFT images.

9. Prototype development and experimental images

An initial laboratory prototype system was developed to confirm the EFT results obtained with FEM simulations. In order to simplify hardware debugging issues, the initial system was designed with one transmit (TX) node and seven receiver (RX) nodes. By keeping the nodes fixed as either a TX or RX node, the system design and electronics was significantly simplified. This, however, meant that tomography data would have to be acquired by manually rotating the sample position. Figure 23 and Figure 24 show the full prototype system with outer shield and displaced capacitive sensor nodes. Figure 25 shows test measurements being taken with a flask of saline solution placed between the transmit and receive nodes. Figure 25 and Figure 27 show the receiver circuit schematic and PCB attached to the shield. Figure 28 shows the Universal Software Radio Peripheral (USRP) data acquisition system which is programmed using the GNU Radio library package. Each USRP system has 4 receiver channels, so the full imaging system will use multiple USRP systems synchronized to an external clock.

Initial measurements on the system indicate that with single receive and transmit channels a phase stability in the order of 20 micro-radians can be obtained. Based on the results we show in Figure 5, this should be more than enough phase stability to detect below 0.5 inch radius plastic objects. The next phase in hardware development is to synchronize multiple USRP systems and acquire tomography data on a full multi channel system.

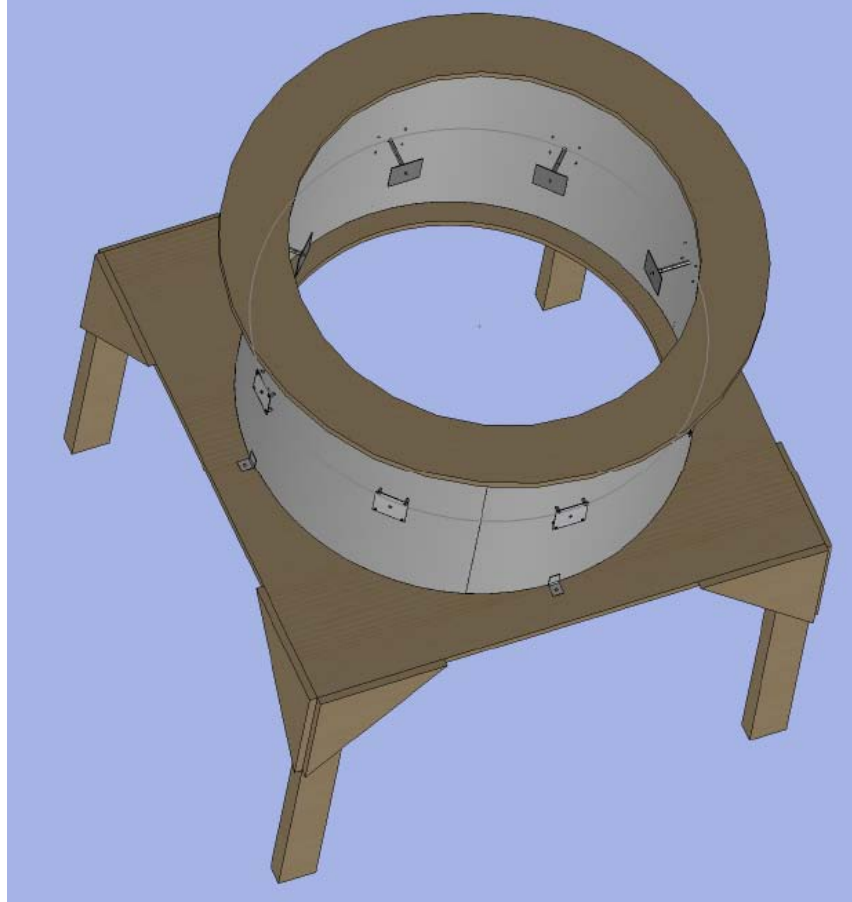


Figure 69. Three-dimensional model of the prototype EFT system with outer shield and capacitive plate sensor nodes.



Figure 70. Shield for prototype system with attached receiver board.



Figure 71. Inside the shield of the EFT system with transmit and receive nodes.

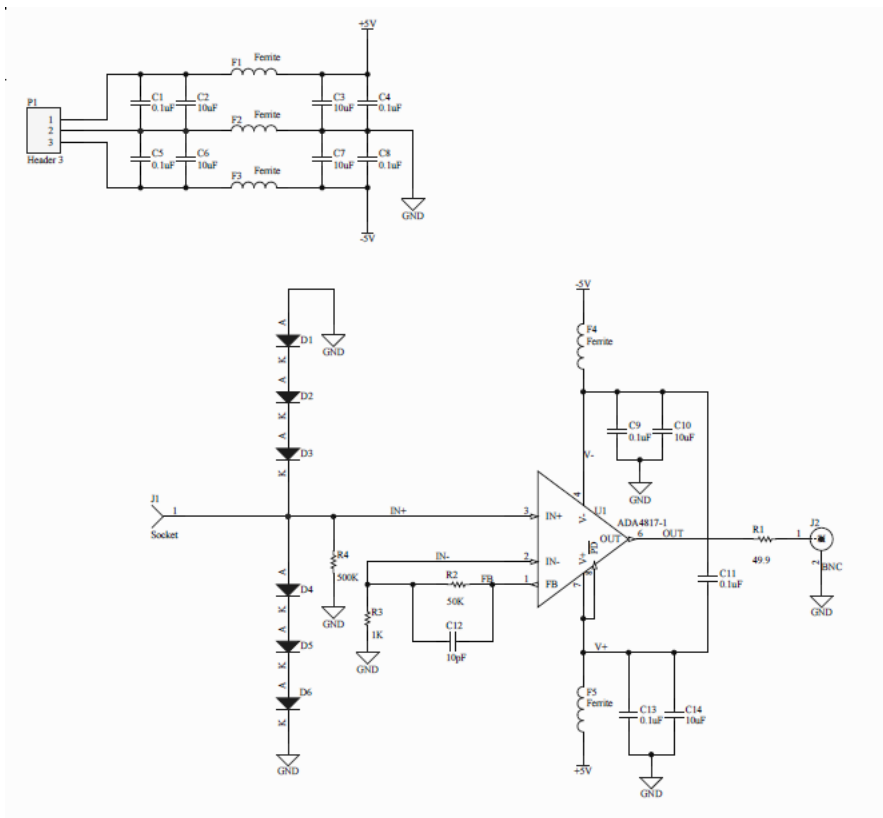


Figure 72. Circuit diagram for the receiver board.

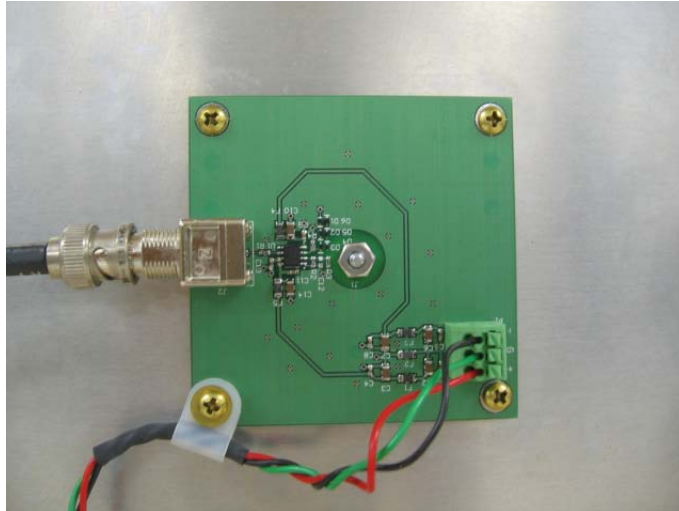


Figure 73. Receiver PCB attached to system outer shield.



Figure 74. USRP data acquisition system.

Figure 29 shows the system setup as tested with the USRP data acquisition modules. Three USRP-1 systems were connected each using 1 channel to digitize the transmit signal and 2-3 remaining receiver channels to digitize the signal from the receiver boards. The comparison of the digitized transmit signal and the receiver signals allow calculation of the phase shift at the receiver nodes due to the presence an imaging sample. An HP-3325A synthesizer is used to generate the transmit signals at frequencies ranging from 1 to 20 MHz. A PTS-160 synthesizer with a Stanford Research System FS73414 distribution amplifier is used to generate an external clock signal to synchronize each of the 3 USRP receiver/digitizers.

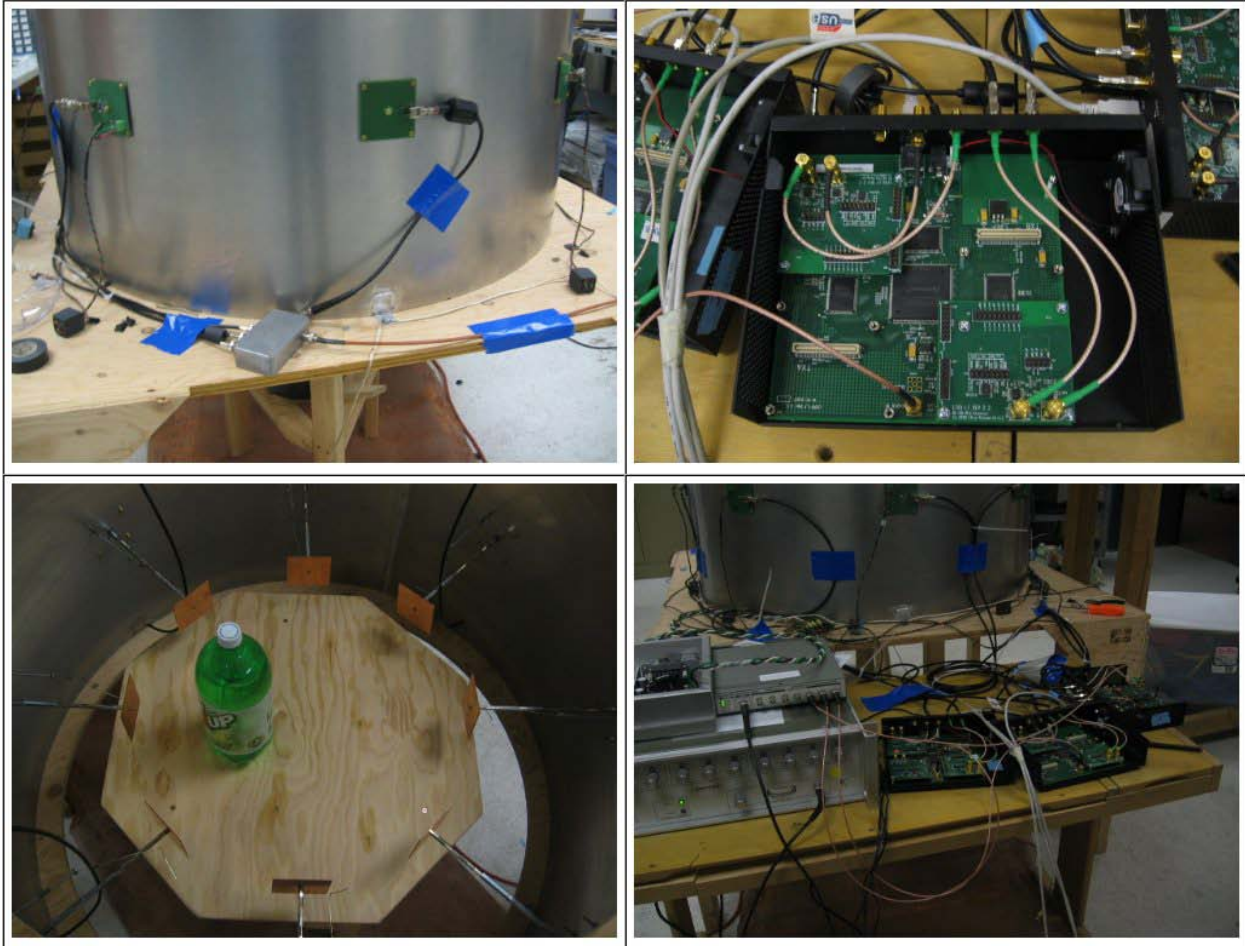


Figure 75. Current lab prototype system configuration.

It was found, however, that the USRP-1 data acquisition modules that were purchased and developed for the tomography system had varying phase distortions in the different channels that were dependent on the signal amplitude. After significant work in testing the USRP systems, it was decided that the phase distortions could not be overcome and a new data acquisition system had to be implemented. Due to time limitations, it was decided to modify an existing in-house spectrometer for the needs of the EFT data acquisition. One limitation with this data acquisition system, however, is that only 4 channels can be acquired at once. Of these, one is always the transmit channel to allow subtraction of the reference signal from the receive signal. Thus in our current system the imaging data must be acquired using sequential sets of 3-channel acquisitions. Figure 30 shows the configuration of the relays to detect the signal from 7 receiver and 1 reference transmitter channel.

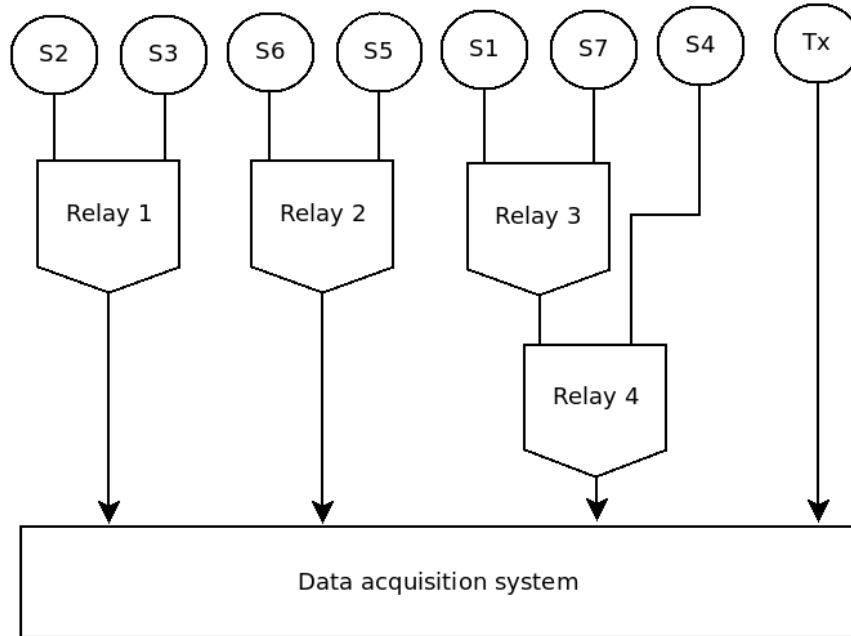


Figure 76. Relay diagram for the data acquisition of signals from 7 receiver sensor nodes and 1 transmit node.

During the debugging process, a GUI program was written to monitor the phase output in real time from the data acquisition system. The program shown in Figure 31 can plot the real and imaginary components from each channel, the phase, and the phase difference with the reference transmit signal subtracted out. This allowed us to monitor the stability of the phase as different components of the hardware was modified. Once the hardware issues had been resolved the system was shown to have better than 100 u-radian stability on all the receiver channels.

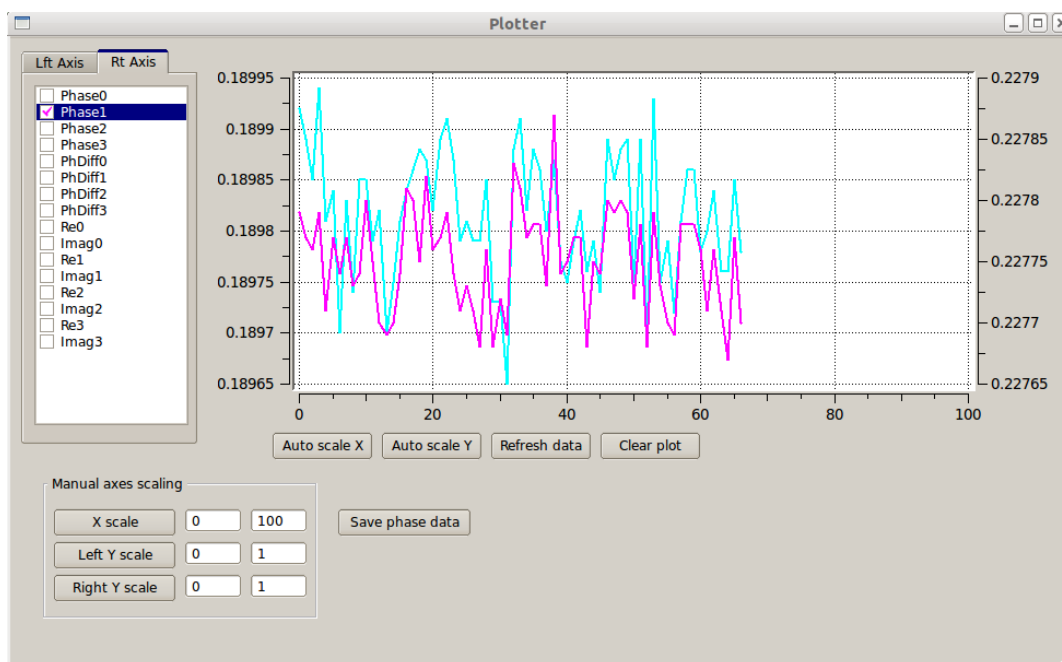


Figure 77. GUI interface for a plotting application to monitor the signal phase in real time.

9.1. Experimental Images

As discussed above, the current system employs 7 fixed receiver sensors and 1 fixed transmitter channel. This setup was used to simplify the debugging procedure; however, in order to obtain the signals from different orientations needed for the image reconstruction, the sample had to be rotated manually through different positions in the imaging region. Figure 32 shows the placement of the sample used to acquire the imaging data. The blue circles represent the 7 receiver sensor nodes and 1 transmitter node; the green circles represent the placement of the sample in 8 different positions used to acquire the imaging data set. These sample placements are equivalent then to the switching of each node between the transmit and receive modes once the transceiver electronics have been implemented. Figure 33 shows the sample in the different radial displacement positions used in the data collection.

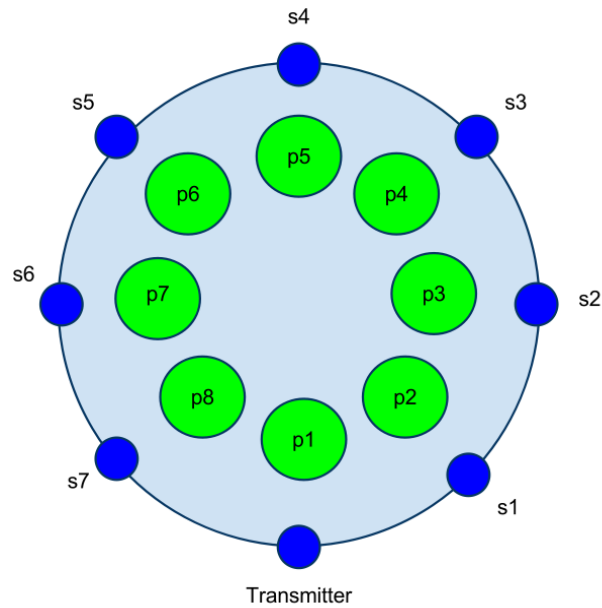


Figure 78. Sample placement *s* used in acquiring imaging data.

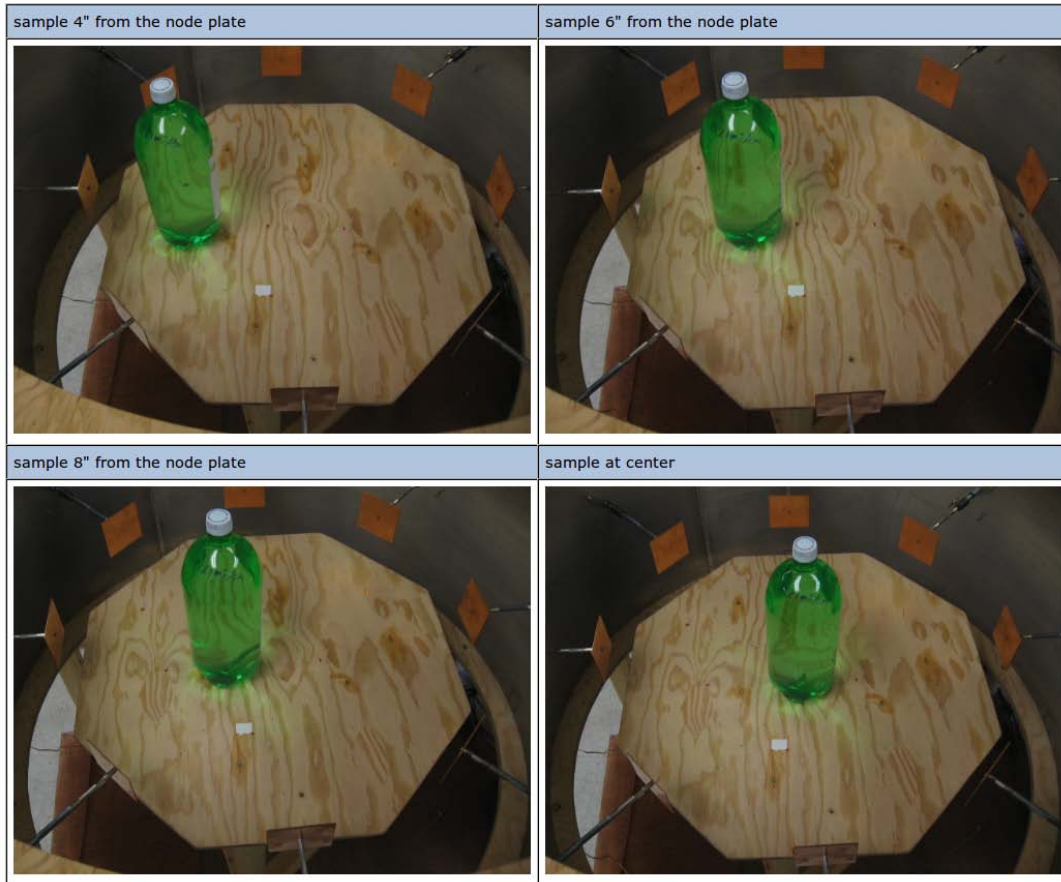


Figure 79. Sample placement at different radial offsets.

Figure 34 and Figure 35 show the comparisons between experiment and simulation of the phase profiles at 5 MHz with a 0.2 mS/cm sample in different positions. These profiles are obtained with the sample at 4" offset from the node plates. The x-axes are labeled with the sensor node numbers. The plot for "position 1" corresponds to the sample located closest to the transmit node, and "position 5" to the sample at the opposite end of the imaging region. Both of these plots should be symmetric about node number 4. The other plots should follow mirror reflection symmetry for position plot pairs (2,8), (3,7), and (4,5). Figure 34 shows that for simulated data these symmetry rules are followed perfectly. These rules were also used initially to determine whether the hardware was behaving as expected, and the failure to follow this symmetry was in fact the initial indication that the USRP data acquisitions system was introducing phase distortions. Figure 35 shows that aside from an overall 180 degree phase shift, the experimental data differ from the simulated data in that the symmetry rules are not followed perfectly. Although the overall shape of the phase profiles do approximately follow the symmetry rules, there are variations in the scaling of the phases that differ from the simulations.

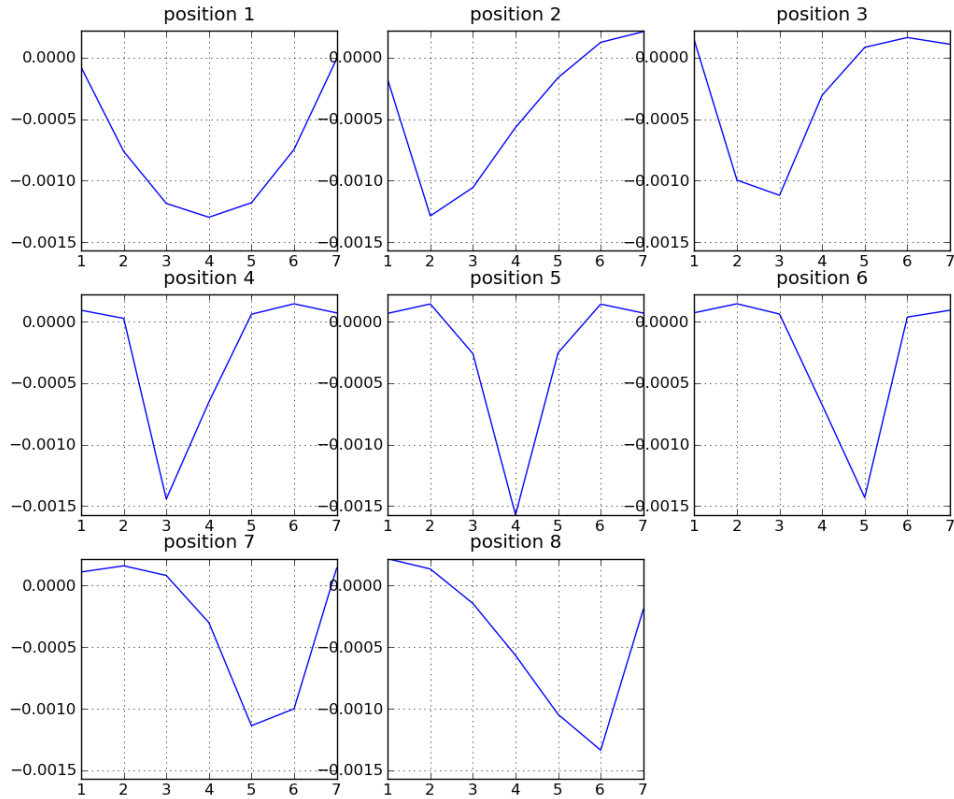


Figure 80. Phase profiles for simulated data.

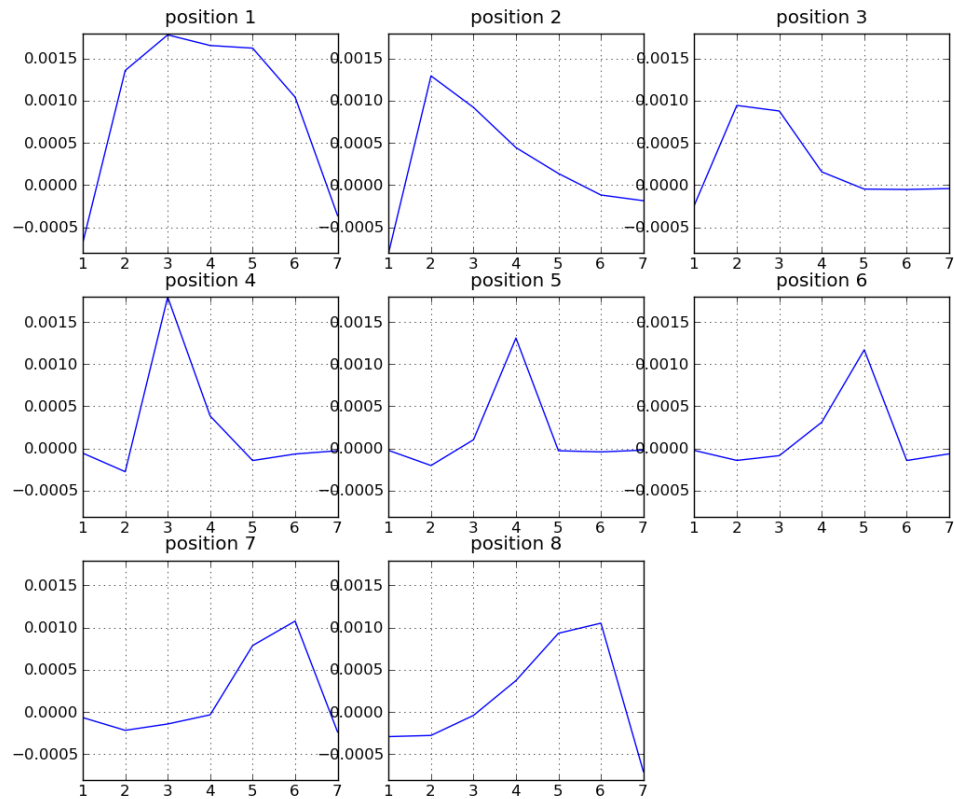


Figure 81. Phase profiles for experimental data.

Despite the differences seen in the phase profiles between experimental and simulated data, the reconstructed images show good agreement the shape of the images between experiment and simulations as shown in Figure 36 and Figure 37. There is, however, a difference in the overall sign of the phase as indicated by the reversal of color coding in the images. The source of difference in the overall phase shift between experiments and simulations is still being investigated. The images were obtained using different radial offsets of the sample placement with respect to the node plates. Both the simulated and experimental images show artifact “rays” due to having only 8 nodes. Figure 38 shows using simulated data the reduction in artifacts that is possible by increasing the number of nodes from 8 to 16.

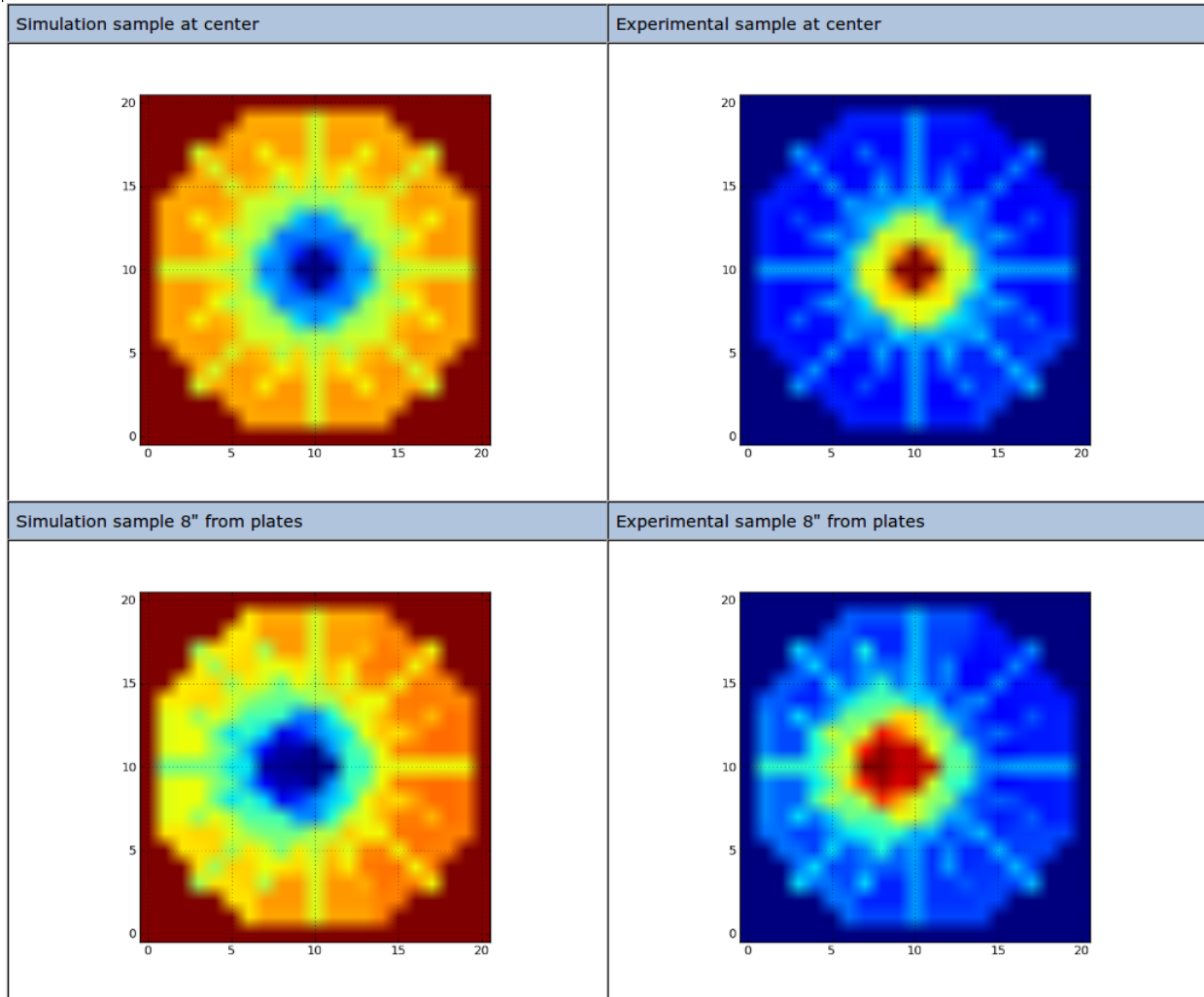


Figure 82. Reconstructed images from simulated and experimental data.

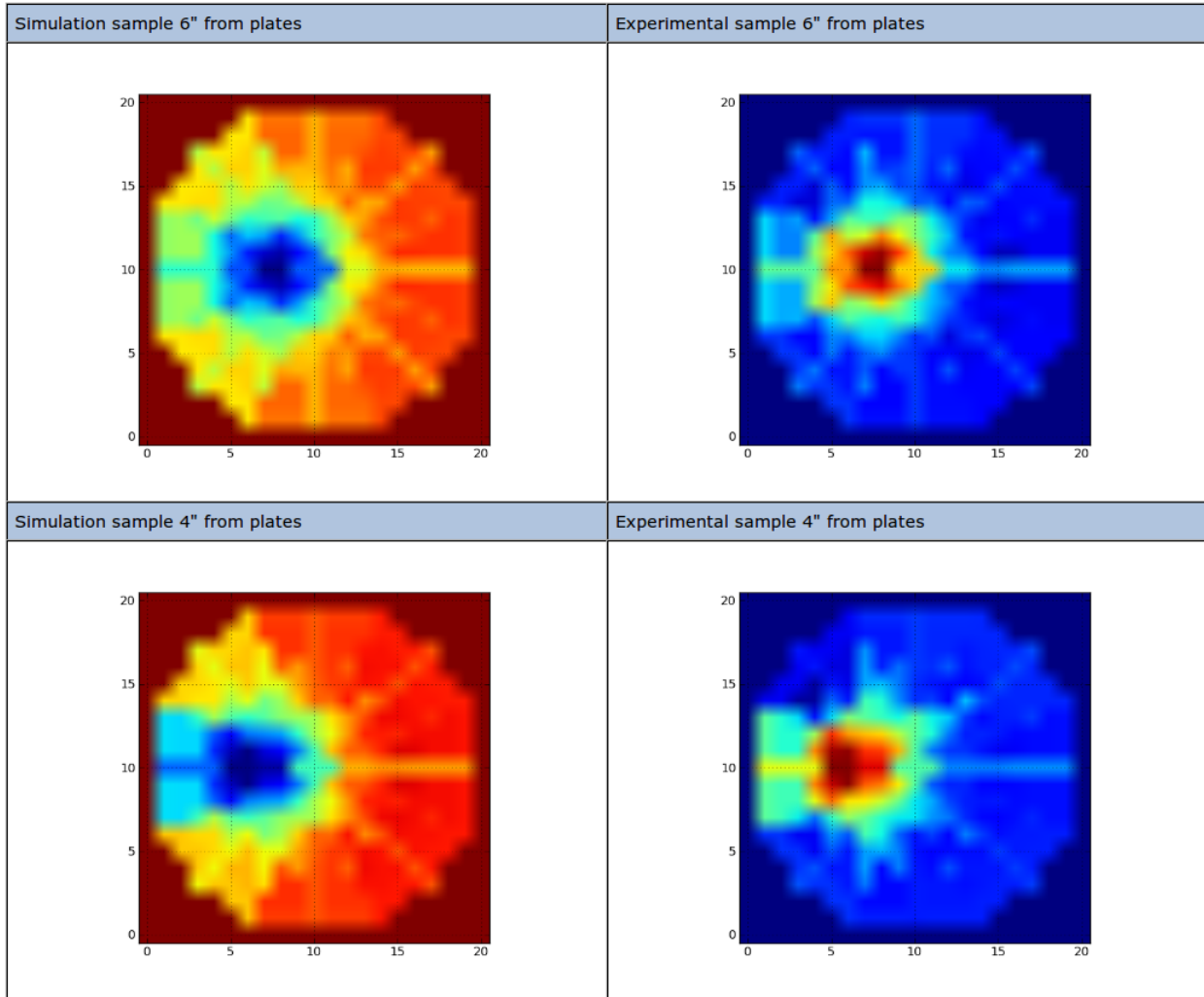


Figure 83. Reconstructed images from simulated and experimental data.

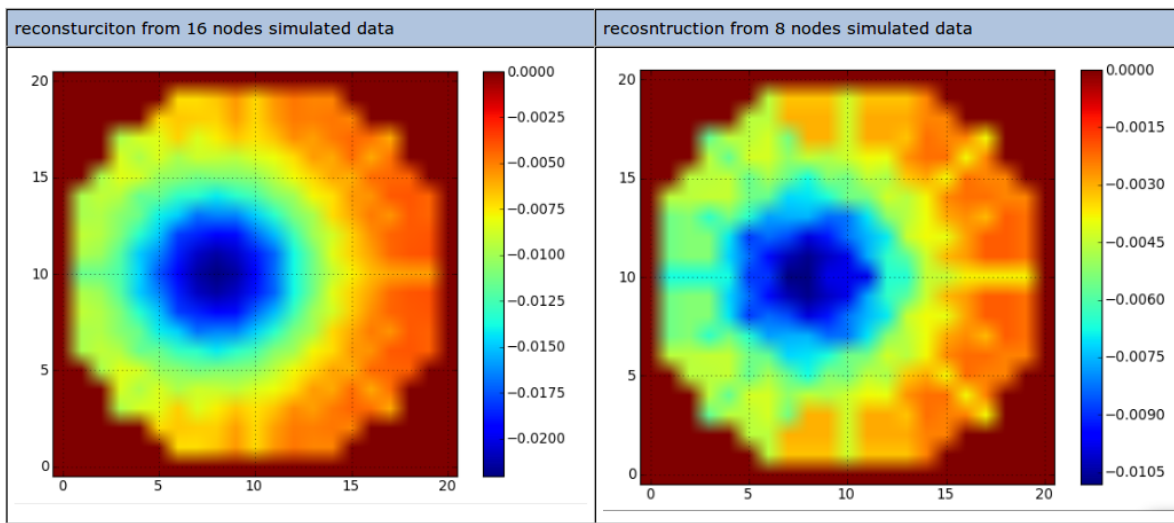


Figure 84. Images from simulated data with 16 and 8 nodes.

10. Experimental multi-frequency images

Upon extending the experimental EFT imaging work from a fixed frequency of 5MHz to varying frequencies ranging from 1 MHz to 20 MHz, several additional technical problems appeared involving noise pickup, stability, and phase artifacts. This section will outline some of these technical problems and solutions implemented or proposed.

Figure 39 shows the node arrangement of the current prototype system. As discussed previously, the nodes are currently fixed as either Transmit or receiver nodes. The figure shows the single transmit node on the system and the numbering of the 7 receiver nodes.

One of the first problems observed when collecting images over a frequency sweep range was what appeared to be oscillations in the image amplitudes. Figure 40 shows the oscillations in phase observed in 2 of the 7 receiver channels within a frequency range of 2 MHz. These oscillations were traced to slight DC offsets seen in each of the 4 digitization channels. There is an overall fixed time delay in the data acquisition system that leads to a frequency dependent phase shift. This shift however is canceled out by digitizing the reference transmit signal and subtracting it from each of the receiver signals. The DC offsets in the digitizer, however are invariant to this frequency dependent phase shift. Thus the DC offsets lead to phase modulations once the digitized transmit and receiver phases are subtracted from each other. This problem was resolved by acquiring the baseline signal on each of the receiver channels with a 50 Ohm load as input to the channels. These signals were then subtracted from the signals acquired with the EFT system. No drift was observed on the DC offsets, so there was no need to update or reacquire the baseline signal.

Figure 41 and Figure 42 show the standard deviations in the phase for 400 background scans acquired at different frequencies ranging from 1 MHz to 20 MHz. With the initial system configuration of an output transmit power of about 4 dBm, it was noticed that the phase standard deviation was dependent on the distance of the receiver node from the transmit node as shown in Figure 41, where curve grouping could be seen for nodes (1,7), (2,6), and (3,5). This was interpreted as the phase stability on each of the channels being determined by the size of the input signal rather than the receiver node electronics. The transmit node was then modified to output signal power of 10 dBm. This increased the stability of the phase detected on the nodes farther from the transmit node as shown in Figure 42; however, their stability was still not to the level of the nearest neighbor receiver nodes 1 and 7. The transceiver nodes have been designed to output significantly higher power than 10 dBm. There are concerns, however, that the increased transmit power could lead to other amplitude dependent phase distortions, and the final output level for the transmit power may require careful balance between phase noise and phase distortions.

As originally designed, shielding from external RF interference (RFI) is provided by a cylindrical aluminum shield 3 ft in height. Experiments at higher frequencies between 10 MHz and 20 MHz show that significant external RFI signals were being picked up on the receiver nodes. Tests using additional shielding as shown in Figure 43 showed that much of the RFI signals could be eliminated as shown by a spectrum analyzer scan in Figure 44. In addition to blocking RFI pickup, the increased shielding seemed to affect the appearance of phase artifacts in images obtained at high frequencies. Figure 45 and Figure 46 show images at varying

frequencies obtained from a sample of .2mS/cm sample placed 4 inches from the node plates. The image sets in Figure 45 were obtained with only the original cylindrical shield; Figure 46 images were obtained with additional shielding of the system. In both cases, images from the sample phantom appear at the lower frequencies as a red/orange circular object left of center. In the case without the additional shielding, another phase image of even greater intensity appears at higher frequencies between 18 MHz and 20 MHz. This image, however, was determined to be an artifact because its position does not change with the placement of the sample. When the shielding was increased, the artifact image was removed as shown in Figure 46. There may, however, still be other artifact images appearing at higher frequencies albeit at lower intensities. Testing continues to examine the effects of shielding and ground planes on the signal phase and reconstructed images with the goal of obtaining reproducible, artifact free images that are modulated fields during the frequency sweep solely due to the interaction of the sample with the electric fields.

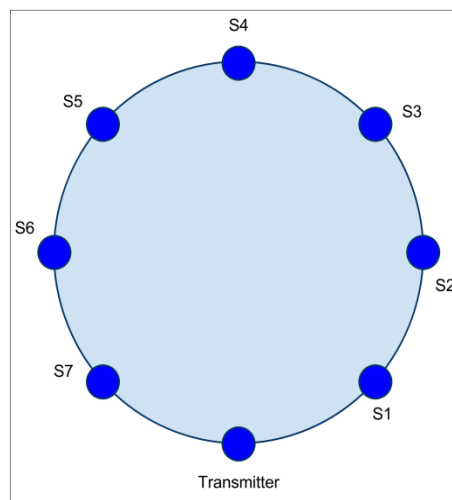


Figure 85. EFT system node arrangement and numbering.

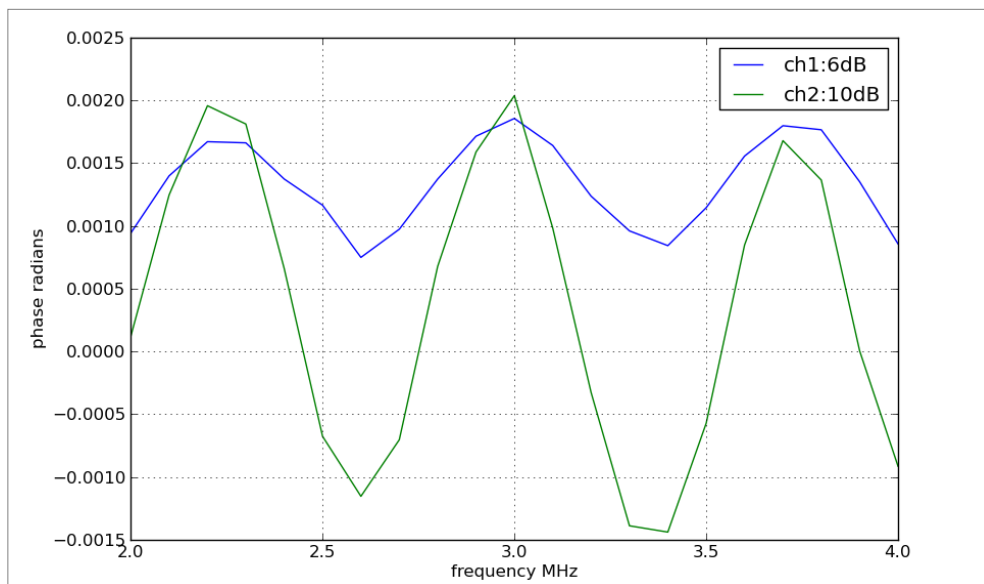


Figure 86. Phase modulations observed during frequency sweeps.

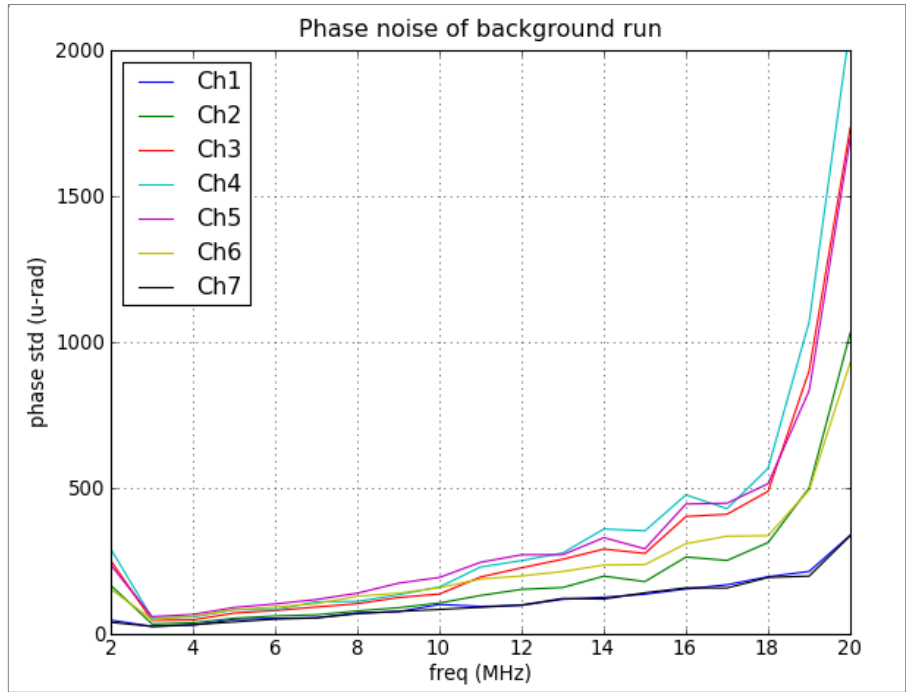


Figure 87. Phase standard deviation with initial configuration with Tx output power of 4 dBm.

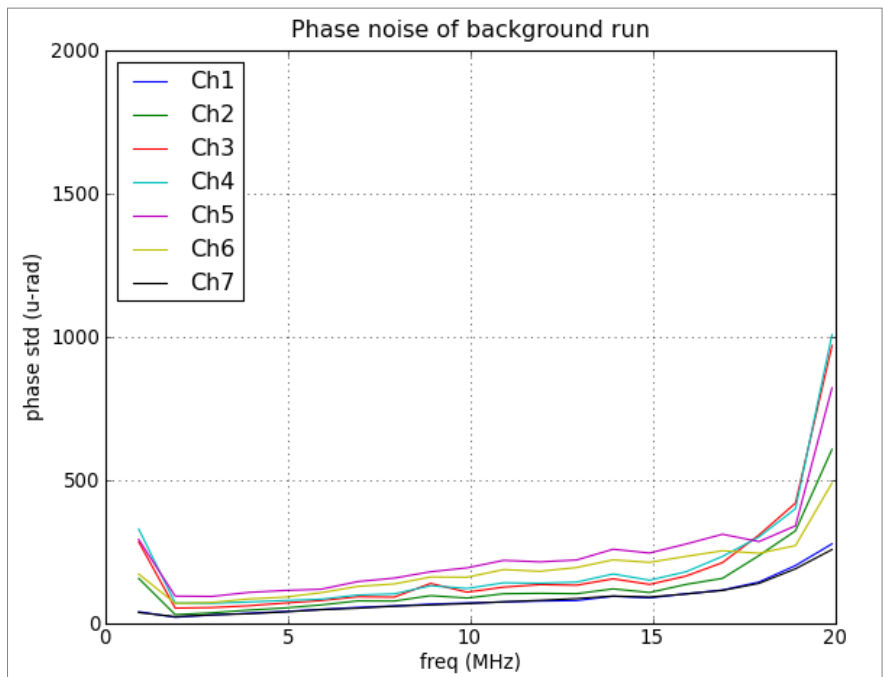


Figure 88. Phase standard deviation with output power of 10dBm.



Figure 89. EFT system being tested with additional shielding.

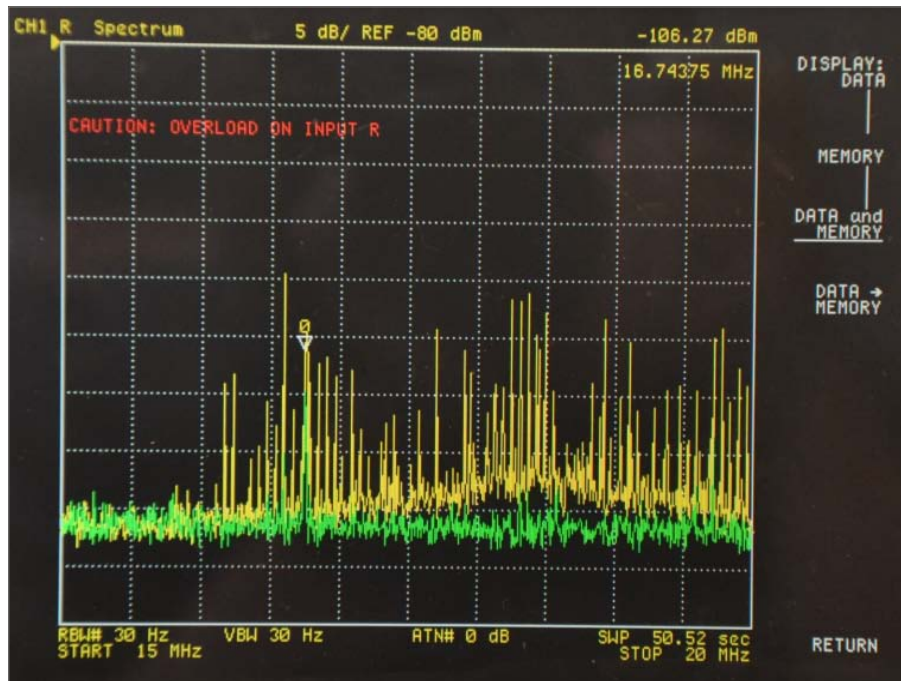


Figure 90. Receiver output measured on a spectrum analyzer with and without additional shielding.

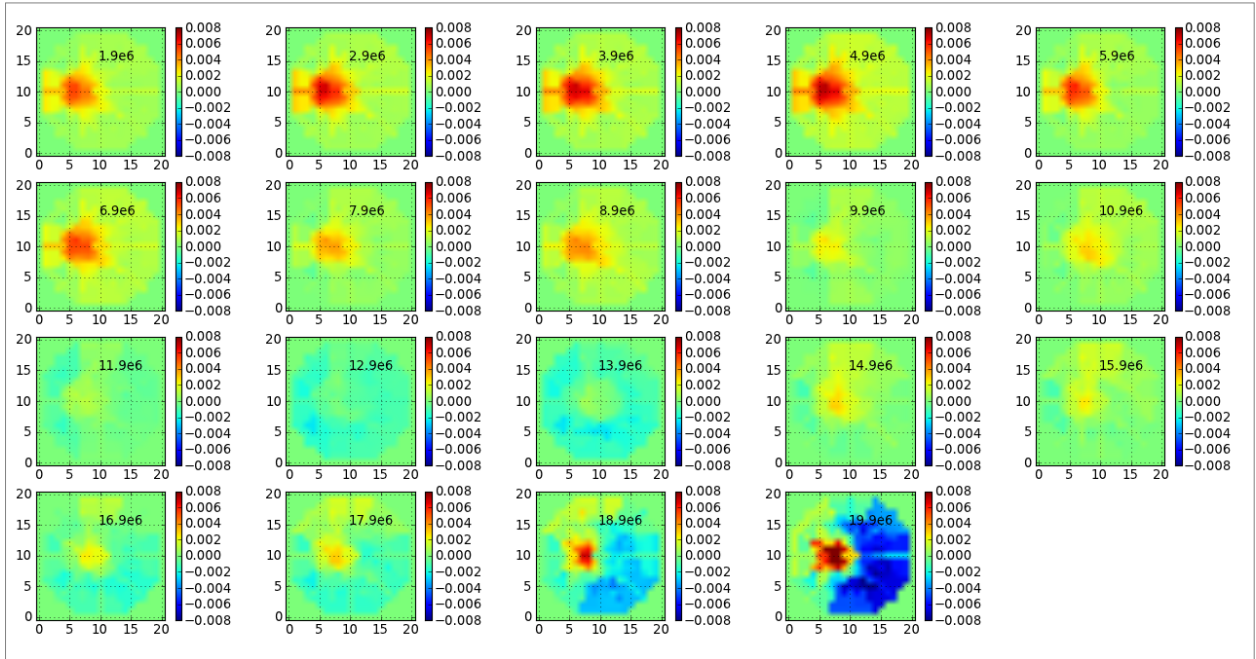


Figure 91. Images obtained at varying frequencies without additional shielding.

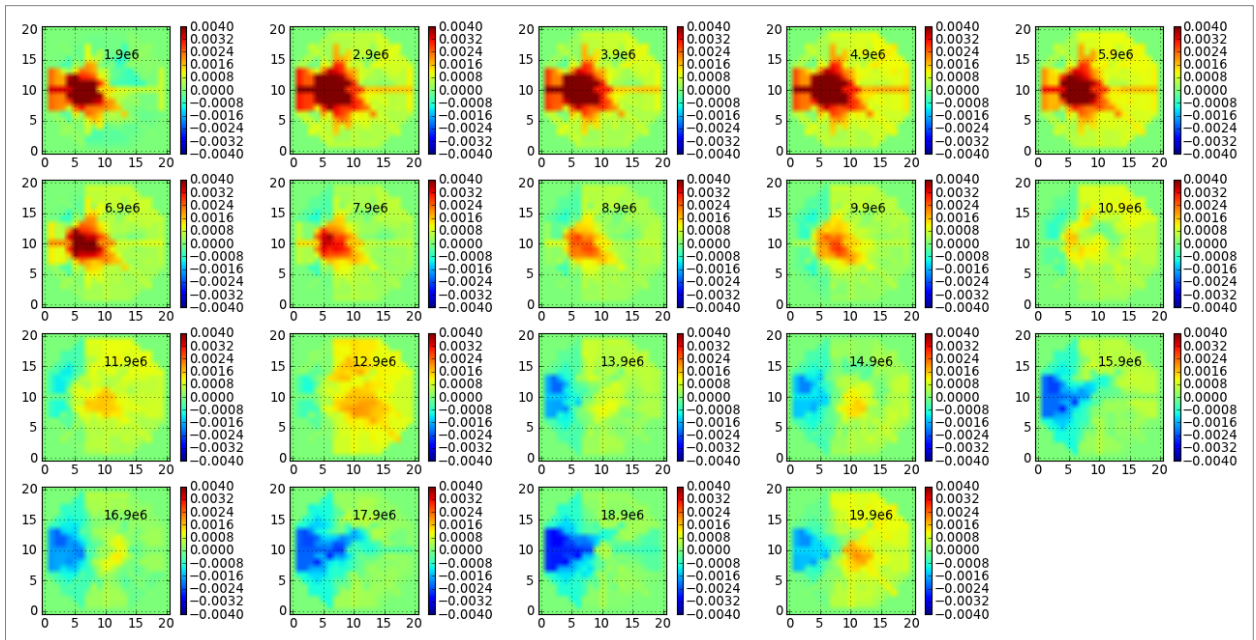


Figure 92. Images obtained at varying frequencies with additional shielding.

11. Design of transceiver node system

As discussed above, a key component missing from the current prototype system is the ability for each node to switch between transmit and receive modes. The current system has a single fixed transmit node with 7 fixed receiver nodes, and thus requires rotation of the sample positions in order to collect a set of data that may be used to reconstruct the image. While this method may be feasible when using phantoms, it becomes hopelessly cumbersome with human subjects. Thus a significant component of the work during the current period of performance was in defining the requirements and designing switchable transceiver node circuits.

A significant effort went into the investigation of alternative amplifier topologies for the receive half of the transceivers. The requirements are:

1. Low noise referred to the input;
2. Low input impedance in the frequency band of interest; and
3. Stability against oscillation.

The first two requirements imply that a charge amplifier will be suitable. Given the high source impedance (the capacitance of the antenna element), the feedback capacitor of the charge amplifier should be small. Given the requirement of low input impedance, the open-loop gain of the amplifier must be very high, which in turn risks causing the amplifier to oscillate (lose stability).

This gives rise to the main challenge: how to achieve all three requirements simultaneously. The topology that lends itself to the first two requirements will, given the frequency band of interest, tend to lead to problems with stability, due to the distributed nature of the antenna. In the band of interest, the antenna may be adequately described as a lumped-parameter capacitor. However, at higher frequencies the antenna becomes electrically large, finally achieving resonance at approximately 200 MHz.

Achieving stability together with the other requirements means that the open loop gain must roll off sharply, so that it is small at frequencies approaching the onset of the antenna resonance. A draft amplifier circuit that promises very low noise was developed and is shown in Figure 47. It is a composite amplifier comprising a JFET (junction-gate field effect transistor) amplifier followed by a high-speed current feedback amplifier configured as a Type I integrator. The network around the current feedback amplifier is designed for stability at high frequencies. Despite the small number of components, the design was extremely challenging because of the need to address competing requirements. Specifically:

1. The input impedance must be < 8 Ohms up to 20 MHz for the phase shift due to the proximity effect (which causes shifts in capacitance of order 1 pF) to be < 1 mrad. Reducing the impedance too far uses up the entire error/noise budget in one place, so a compromise impedance is < 2 Ohms.
2. Given a source capacitance of order 10 pF, one cannot use a feedback capacitor much greater than 10 pF without yielding an unacceptable noise gain.

- This, in turn, means that a gain-bandwidth product of 8 GHz is required. The JFET amplifier by far best-suited for this application, the ADA4817, has only 400 MHz gain-bandwidth product, forcing a gain of 20 at 20 MHz.

This high-gain requirement forces the composite amplifier approach of Figure 47. The risk of amplifier oscillation is high without extensive design iterations and layout iterations to control variations in stray capacitance, and the like. If oscillations can be suppressed, it should provide <math><5.3\ \text{Ohms}</math> up to 10 MHz, still short of the design goal but better than all known or conceived alternatives. However, paper designs are based on datasheets and models that give unreliable approximations at the gains and frequency limits required of the present application, further increasing the risk.

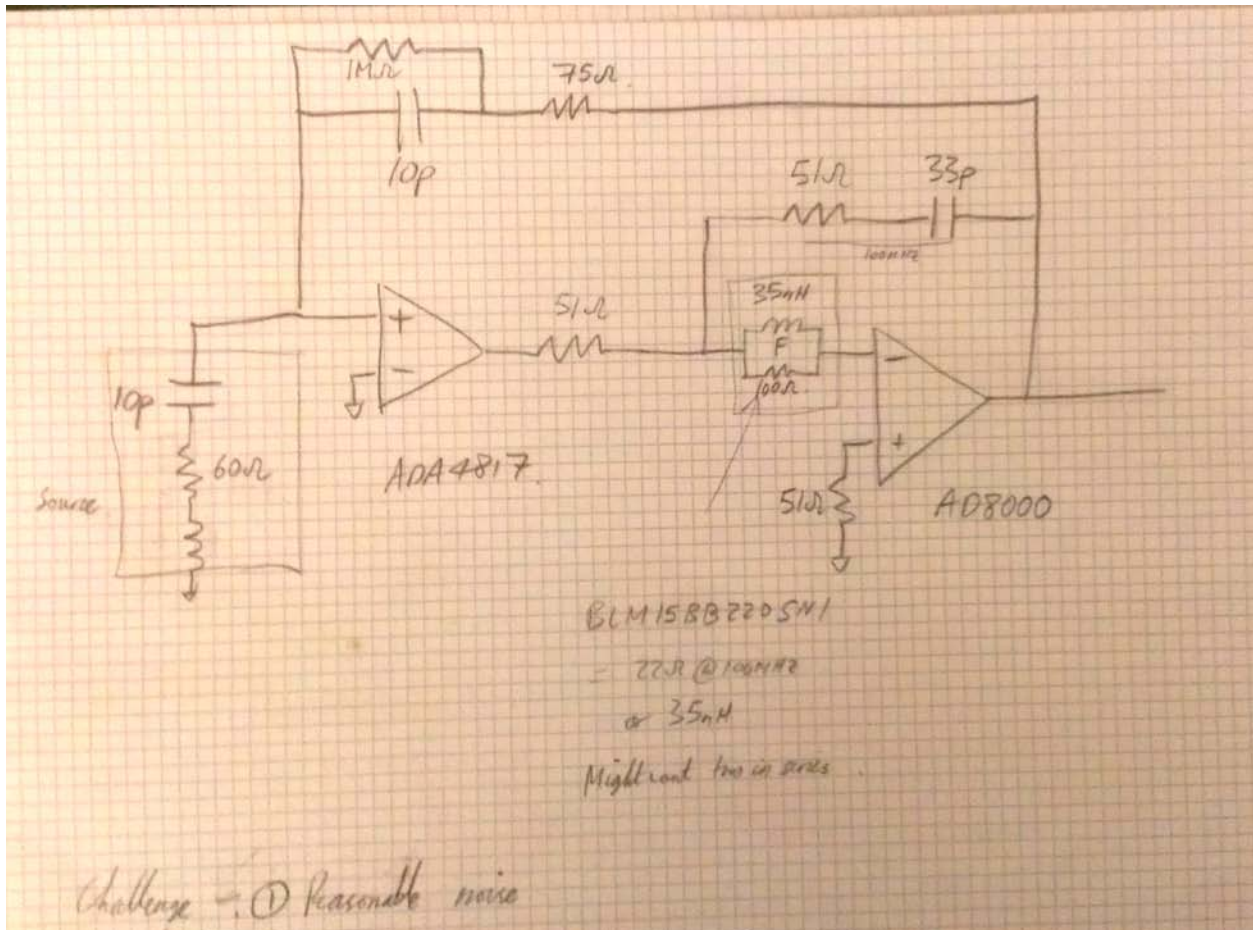


Figure 47. Study schematic of an advanced charge amplifier circuit topology.

Because of limited funds and time, it was decided, following this investigation of alternative amplifier topologies, to focus on the integration and automation of the data acquisition electronics, in the form of relay-controlled transceiver nodes, using the amplifier design existing from the previous work. This amplifier offers the virtues of known stability and thorough characterization over the frequency band of interest, even though its phase noise performance does not meet ultimate requirements.

Should there be time and funding in the following phase of work, the amplifier design may be revisited. Furthermore, shortening the antennas will improve stability by raising their resonant

frequencies, moving the resonances farther from the frequency band of interest. This, however, may come with a loss of sensitivity. Clearly, the parameter space is large; but advanced amplifier design is the most likely avenue to a future breakthrough in contraband detection sensitivity and image resolution.

The transceiver and RF switching circuits as well as the PCB layouts have been completed. A general block diagram for the transceiver node system is shown in Figure 48. The present data acquisition system can digitize 4 channels in parallel. Of those, one channel must always be the reference transmit signal. Thus, for the present 8-node system, signals from 7 receive channels can be acquired with 3 sequential data acquisition periods. The diagram in Figure 48 is labeled for an 8-node system; however, the components allow easy extension up to 12 nodes (requiring 4 sequential data acquisition periods for 11 receiver nodes). By having each node switch between receive and transmit modes, the electrical circuits for the nodes become significantly more complicated than the circuits originally implemented.

Transceiver circuit board layouts and masks are shown in Figures 49 through 54. Figures 55 and 56 show power and relay circuit board layouts and masks.

Physical implementation of the transceiver nodes will be done during the next phase of the project.

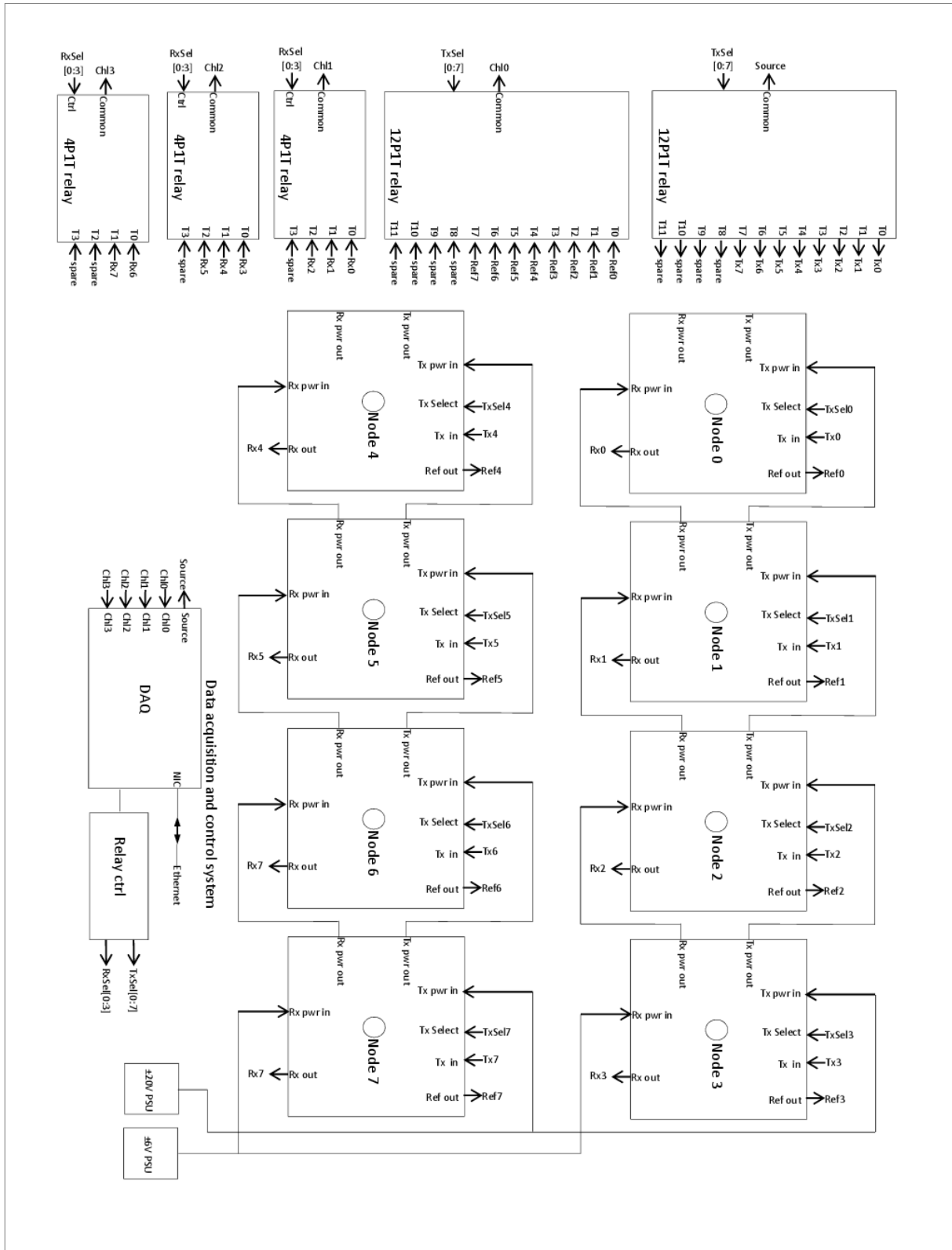


Figure 48. EFT system diagram with transceiver nodes.

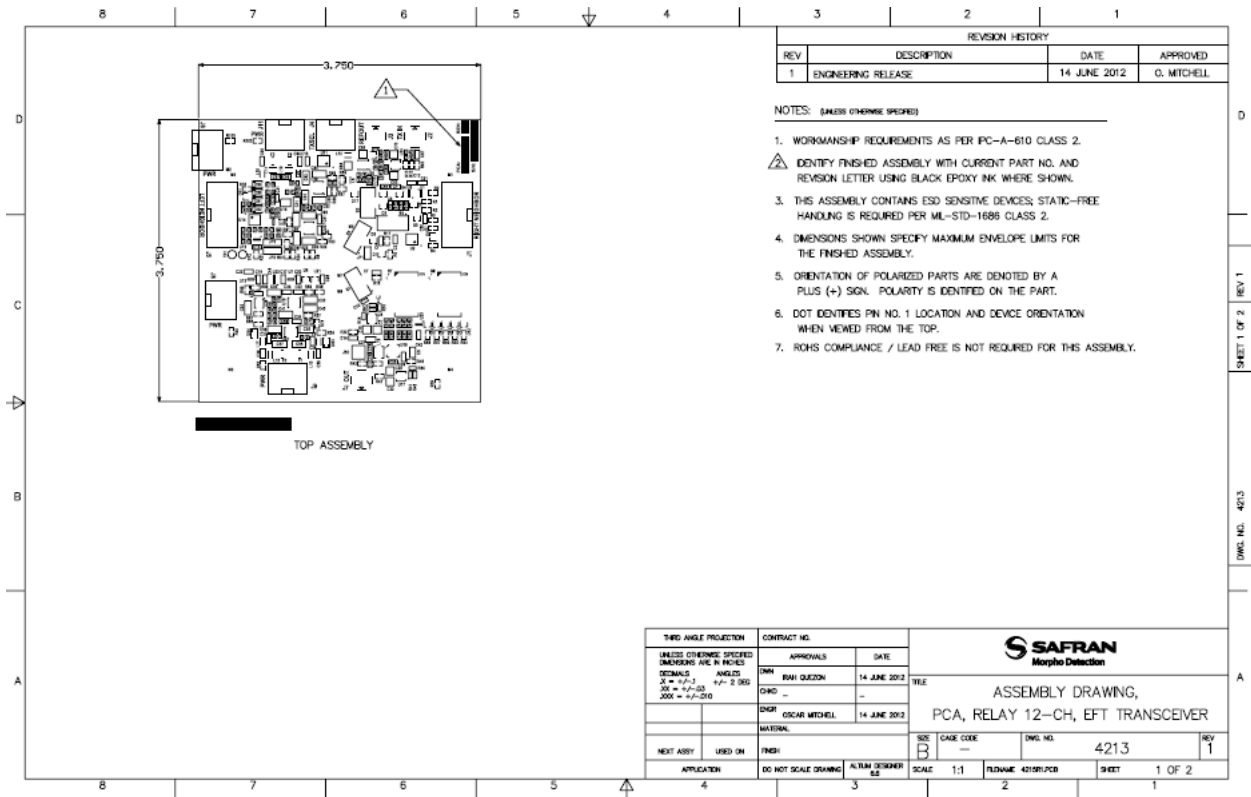
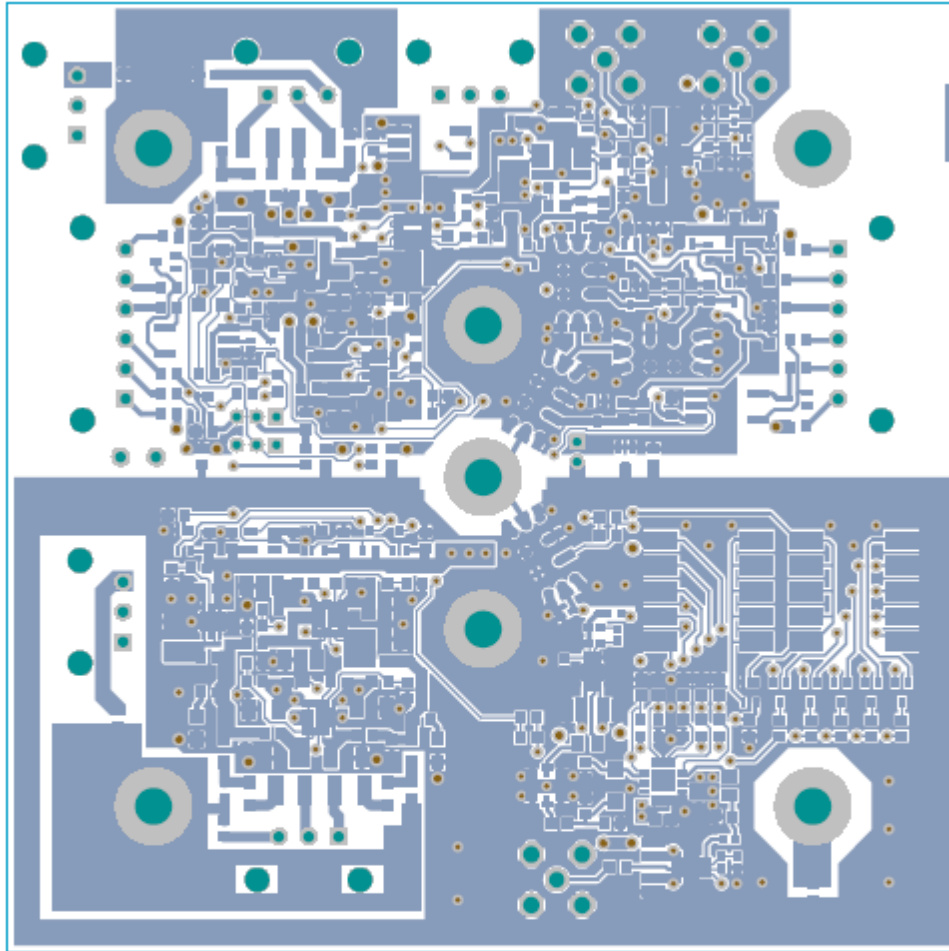


Figure 49. Transceiver layout (component side).



PRODUCTION MASTER

TOP, LAYER 1 (GTL)

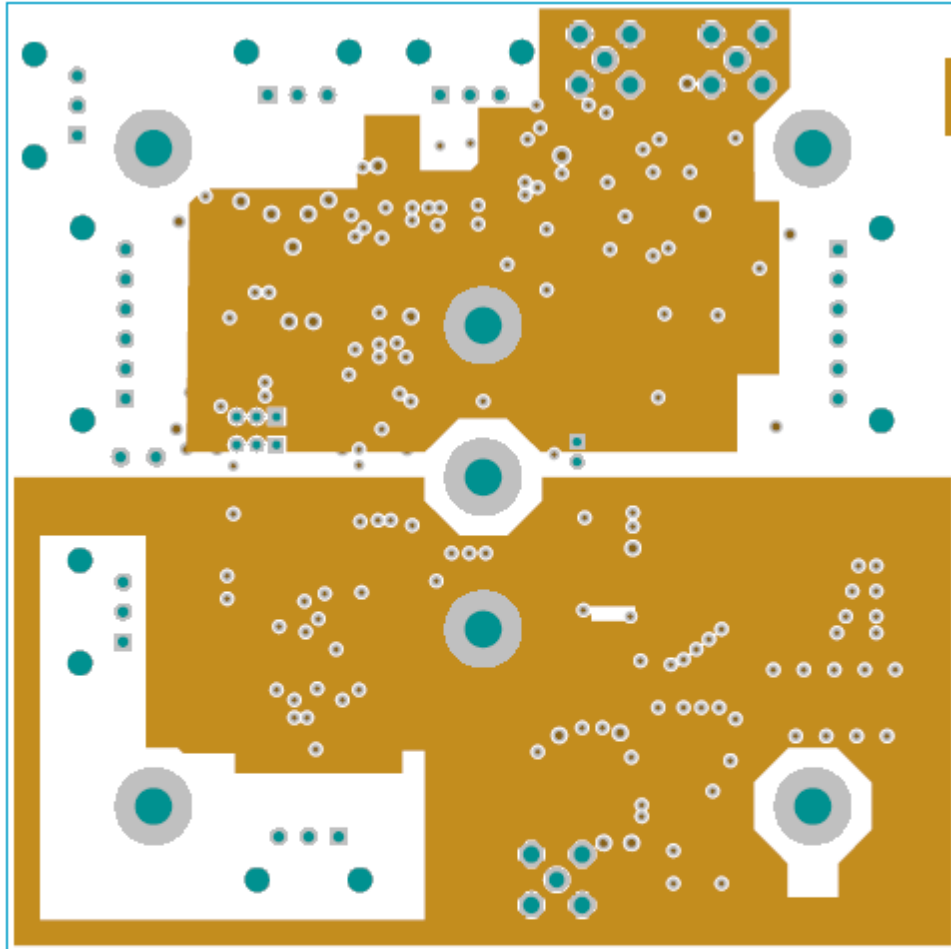
PN 4215 REV 1

PCB, TRANSCEIVER, EFT NODE CARRIER

MORPHO DETECTION (SAFRAN GROUP)

14 JUNE 2012

Figure 50. Transceiver top layer board mask.



PRODUCTION MASTER

GND, LAYER 2 (.G1)

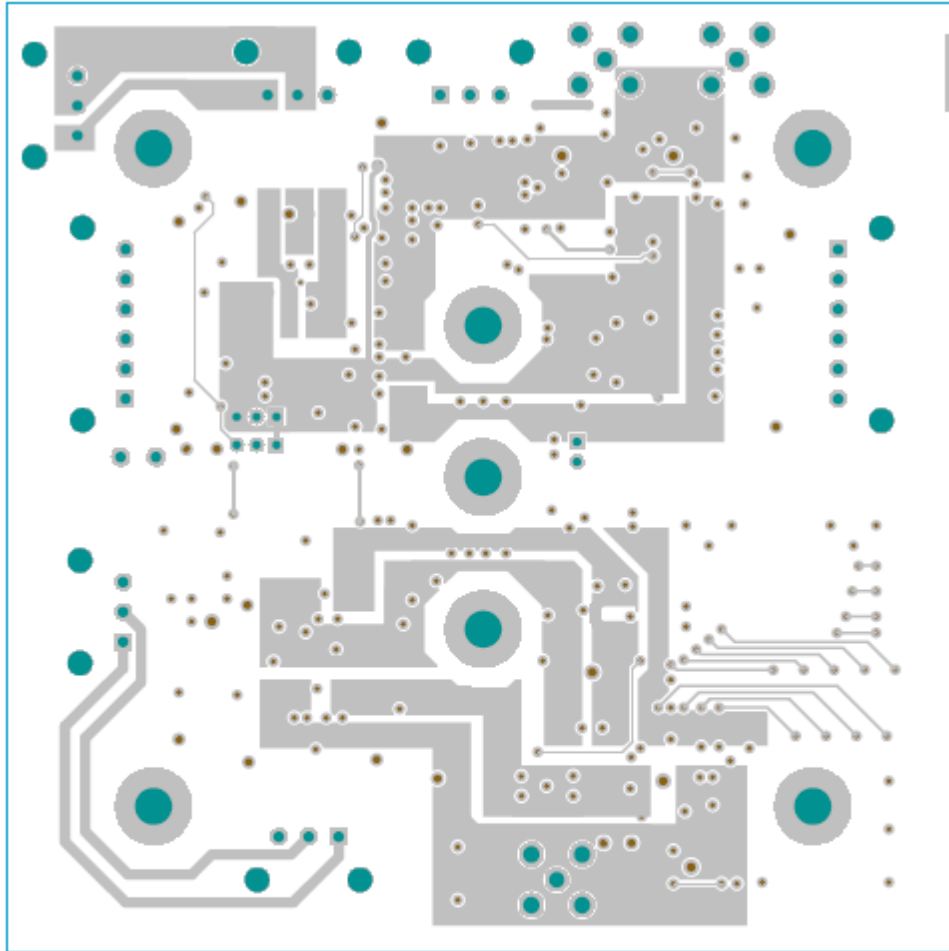
PN 4215 REV 1

PCB, TRANSCEIVER, EFT NODE CARRIER

MORPHO DETECTION (SAFRAN GROUP)

14 JUNE 2012

Figure 51. Transceiver ground layer board mask.



PRODUCTION MASTER

MID, LAYER 3 (.G2)

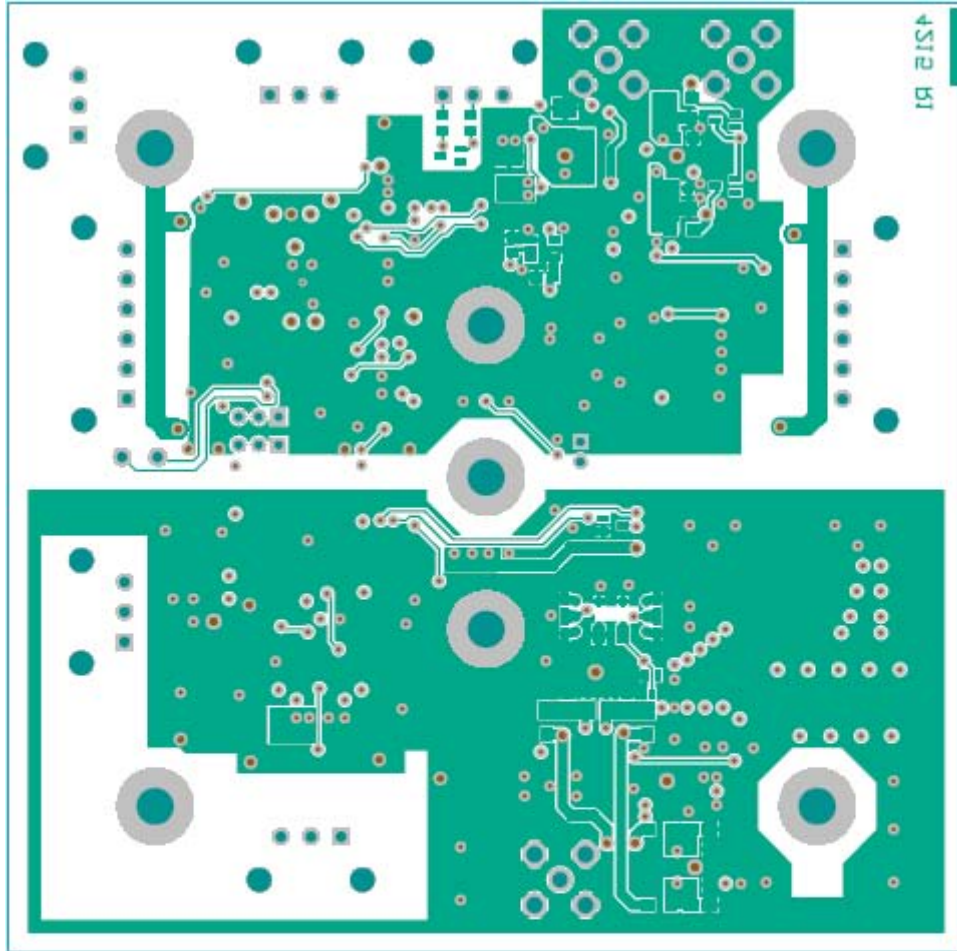
PN 4215 REV 1

PCB, TRANSCEIVER, EFT NODE CARRIER

MORPHO DETECTION (SAFRAN GROUP)

14 JUNE 2012

Figure 52. Transceiver third layer board mask.



PRODUCTION MASTER

BOTTOM, LAYER 4 (.GEL)

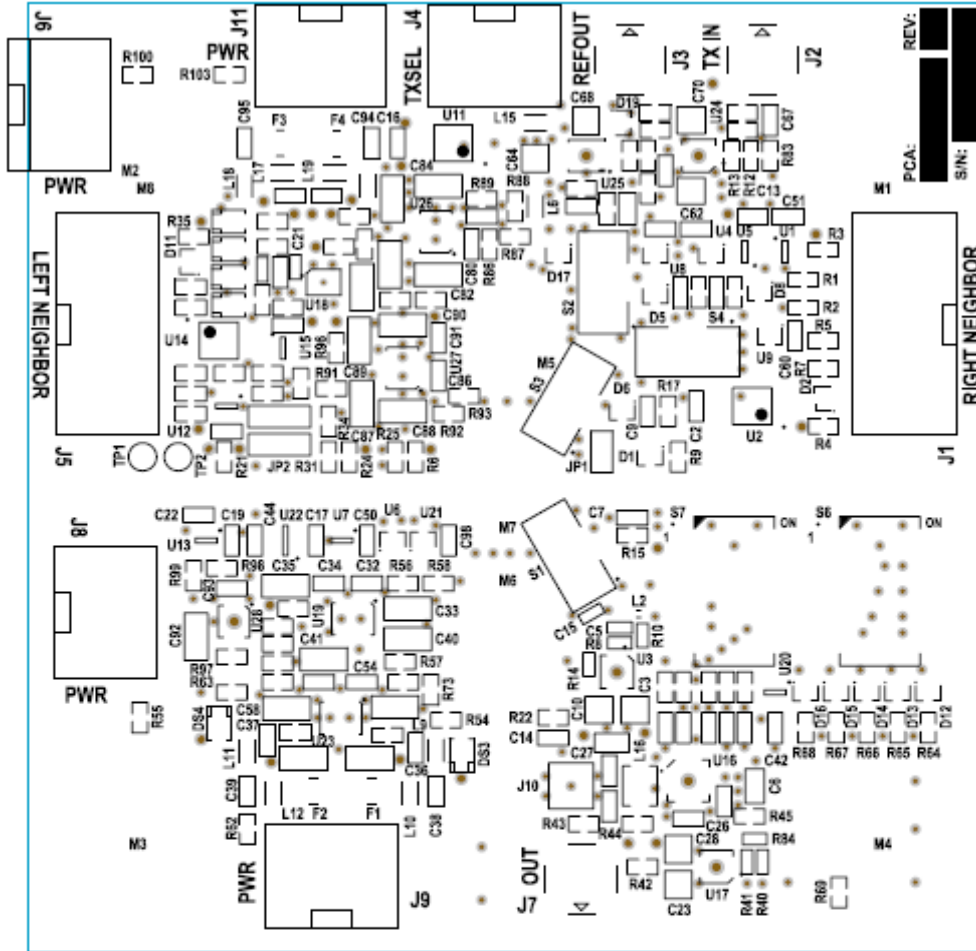
PN 4215 REV 1

PCB, TRANSCEIVER, EFT NODE CARRIER

MORPHO DETECTION (SAFRAN GROUP)

14 JUNE 2012

Figure 53. Transceiver bottom (fourth) layer board mask.



PRODUCTION MASTER
TOP SILKSCREEN (.GTO)

PN 4215 REV 1
PCB, TRANSCEIVER, EFT NODE CARRIER
MORPHO DETECTION (SAFRAN GROUP)
14 JUNE 2012

Figure 54. Transceiver board component layout silk screen.

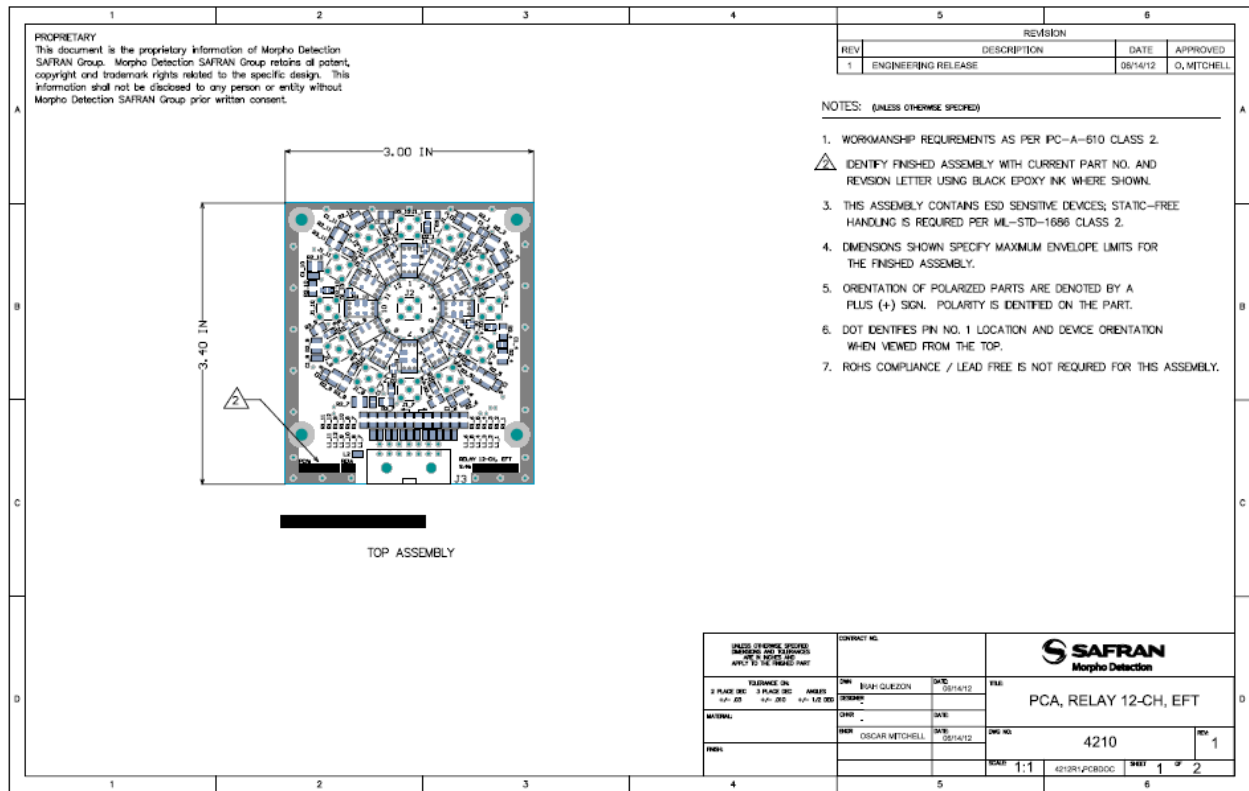
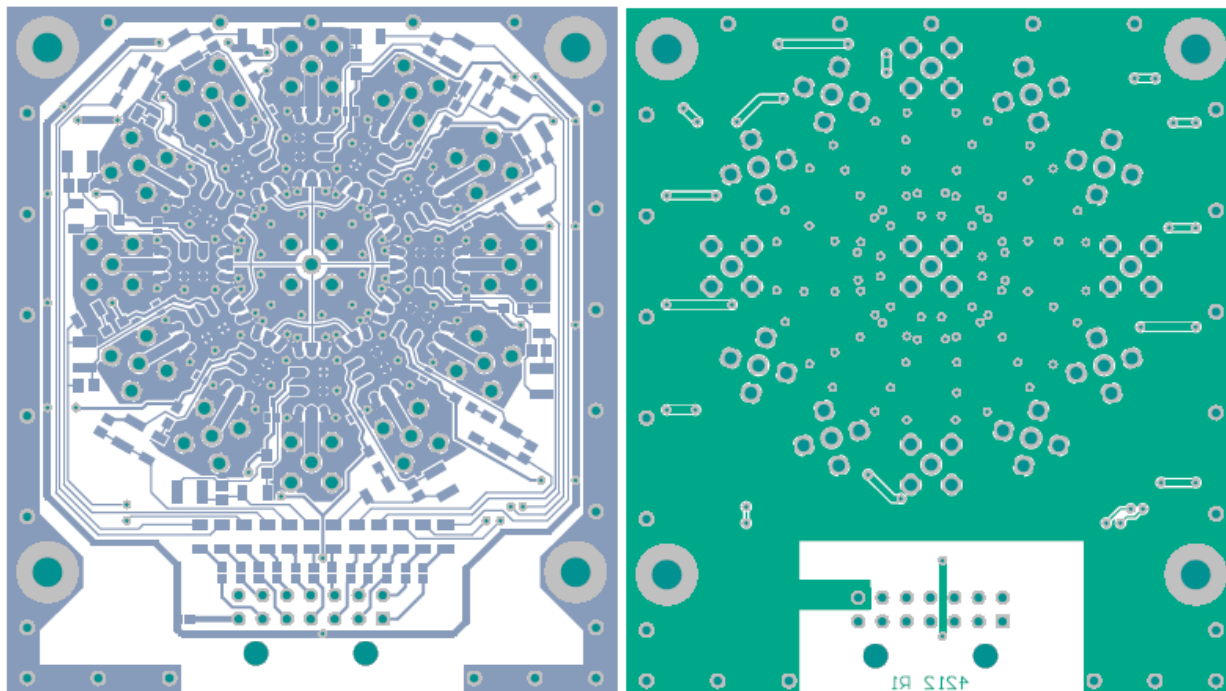


Figure 55. Relay board layout (component side).



PRODUCTION MASTER
PRIMARY SIDE, LAYER 1 (.GTL)

PN 4212 R1
PCB, RELAY 12-CH, EFT
MORPHO DETECTION (SAFRAN GROUP)
06/14/12

PRODUCTION MASTER
SECONDARY SIDE, LAYER 2 (.GBL)

PN 4212 R1
PCB, RELAY 12-CH, EFT
MORPHO DETECTION (SAFRAN GROUP)
06/14/12

Figure 56. Relay board masks.